Probabilistic Quantification of Tsunami Currents in Karachi Port, Makran Subduction Zone, using Statistical Emulation

Devaraj Gopinathan[1,1], Mohammad Heidarzadeh[2,2], and Serge Guillas[1,1]

[1]University College London
[2]Brunel University London
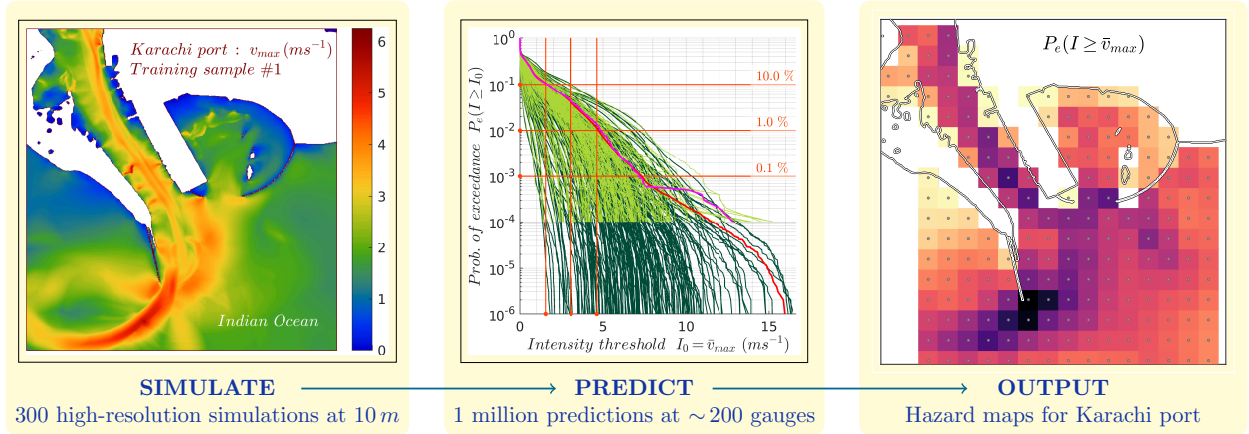
November 30, 2022

Abstract

In this paper, we model the full range of possible local impacts of future tsunamis in the Makran subduction zone (MSZ) at Karachi port, Pakistan. For the first time, the 3-D subduction geometry Slab2 is employed in the MSZ, in conjunction with the most refined rupture segmentation to date for this region, to improve the earthquake source definition. Motivated by the massive sediment layer over the MSZ, we also introduce to tsunami modeling the application of the sediment amplification formula, resulting in enhancements of seabed deformation up to 60% locally. Furthermore, we design a new unstructured mesh algorithm for our GPU-accelerated tsunami code in order to efficiently represent flow velocities, including vortices, down to a resolution of 10m in the vicinity of the port. To afford to compute very large number of high resolution tsunami scenarios, for the granularity and extent of the range of magnitudes (occurrence ratios of 1:100,000 implied by the Gutenberg-Richter relation) and locations of source, we create a statistical surrogate i.e. emulator) of the tsunami model. Our main contribution is hence the largest set of emulated predictions using any realistic tsunami code to date: 1 million per location. We go on to obtain probabilistic representations of maximum tsunami velocities and heights at around 200 locations in the port area of Karachi. Amongst other findings, we discover substantial local variations of currents and heights. Hence we argue that an end-to-end synthesis of advanced physical, numerical and statistical modeling is instrumental to comprehensively model local impacts of tsunamis.

1

1 Graphical Abstract

2 Probabilistic Quantification of Tsunami Currents in Karachi Port, Makran Subduction Zone,
3 using Statistical Emulation

4 Devaraj Gopinathan,Mohammad Heidarzadeh,Serge Guillas

SIMULATE
300 high-resolution simulations at $10\,m$

PREDICT
1 million predictions at ~ 200 gauges

OUTPUT
Hazard maps for Karachi port

Highlights

Probabilistic Quantification of Tsunami Currents in Karachi Port, Makran Subduction Zone, using Statistical Emulation

Devaraj Gopinathan,Mohammad Heidarzadeh,Serge Guillas

- First hazard maps of port currents using 1 million scenarios (at $10\,m$ resolution)
- Greater than $50\,\%$ variation in velocities at harbor's mouth
- Maximum exceedance $\sim 18/10/4\,\%$ for velocities $\sim 1.5/3/4.5\,ms^{-1}$ respectively
- Maximum velocities $\sim 3/7.5/10\,ms^{-1}$ for exceedance $10/1/0.1\,\%$ respectively
- Up to $60\,\%$ seabed deformation amplification due to sediments

Probabilistic Quantification of Tsunami Currents in Karachi Port, Makran Subduction Zone, using Statistical Emulation

Devaraj Gopinathan[a,*], Mohammad Heidarzadeh[b] and Serge Guillas[a]

[a]*Department of Statistical Science. University College London, Gower Street, London WC1E 6BT, UK.*

[b]*Department of Civil & Environmental Engineering. Brunel University London, Uxbridge UB8 3PH, UK.*

ABSTRACT

In this paper, we model the full range of possible local impacts of future tsunamis in the Makran subduction zone (MSZ) at Karachi port, Pakistan. For the first time, the 3-D subduction geometry Slab2 is employed in the MSZ, in conjunction with the most refined rupture segmentation to date for this region, to improve the earthquake source definition. Motivated by the massive sediment layer over the MSZ, we also introduce to tsunami modeling the application of the sediment amplification formula, resulting in enhancements of seabed deformation up to 60 % locally. Furthermore, we design a new unstructured mesh algorithm for our GPU-accelerated tsunami code in order to efficiently represent flow velocities, including vortices, down to a resolution of $10\,m$ in the vicinity of the port. To afford to compute very large number of high resolution tsunami scenarios, for the granularity and extent of the range of magnitudes (occurrence ratios of $1 : 100,000$ implied by the Gutenberg-Richter relation) and locations of source, we create a statistical surrogate (*i.e.* emulator) of the tsunami model. Our main contribution is hence the largest set of emulated predictions using any realistic tsunami code to date: 1 million per location. We go on to obtain probabilistic representations of maximum tsunami velocities and heights at around 200 locations in the port area of Karachi. Amongst other findings, we discover substantial local variations of currents and heights. Hence we argue that an end-to-end synthesis of advanced physical, numerical and statistical modeling is instrumental in coastal engineering to comprehensively model local impacts of tsunamis.

1. Introduction

Destructive tsunami currents in ports have attracted the attention of coastal engineering community in recent years (Park and Cox, 2016). Following the unexpected damage incurred at ports from the tsunamis of 2004 (Indian Ocean), 2010 (Chile) and 2011 (Japan) (Borrero et al., 2015b; Okal et al., 2006), it is of paramount importance to investigate the associated hazard. Ports are vital economic lifelines and thus need to be safeguarded from natural disasters to prevent *e.g.* a sudden interruption of trade and commerce, a halt in the flow of essential commodities, as well as the destruction of livelihoods of fishermen communities. Despite recent studies (Borrero et al., 2015a,b; Lynett et al., 2012, 2014) and advances in high-fidelity modeling (Lynett et al., 2017), probabilistic methods tackling the quantification of future tsunami hazard due to strong flows in harbors are sparse (Park and Cox, 2016; Gonzalez et al., 2013). The need for such probabilistic quantifications is further accentuated by certain peculiarities that were observed with the phenomena of tsunami currents in ports. On 26 December 2004, the Sumatra-Andaman (SA) tsunami waves at the Omani port of Salalah wrested the freighter *Maersk Mandraki* from the main wharf before it was shoved around by the

---

*Corresponding author

✉ d.gopinathan@ucl.ac.uk (D. Gopinathan); mohammad.heidarzadeh@brunel.ac.uk (M. Heidarzadeh); s.guillas@ucl.ac.uk (S. Guillas)

ORCID(s): 0000-0002-0490-3229 (D. Gopinathan); 0000-0002-1112-1276 (M. Heidarzadeh); 0000-0002-3910-3408 (S. Guillas)

54 vortices induced from the tsunami currents (Okal et al., 2006). The 285 *m* long ship drifted uncontrollably for hours,

55 despite manual intervention (Figure 1). It looped both inside and outside the harbor prior to winding up on a sand bar.

56 Another anomaly was observed on 24 September 2013, when a submarine landslide in the Makran subduction zone

57 (MSZ) generated a tsunami in the North-Western (NW) Indian Ocean, affecting the coasts of Oman, Iran, Pakistan

58 and India (Heidarzadeh and Satake, 2014). The landslide that caused the tsunami was the secondary effect of a small

59 M_w 7.7 inland strike-slip earthquake. Tide-gauge records displayed tsunami waves of small amplitude ($20 \pm 7\,cm$) in

60 the affected regions, except for three Omani ports (Heidarzadeh and Satake, 2014, Table 1 & Figure 3). Relatively

61 larger amplitudes were found in the ports of Muscat ($51\,cm$), Quarayat ($109\,cm$) and Sur ($40\,cm$). Here, the waves also

62 prevailed for a relatively longer duration ($\gtrsim 6\,h$) compared to the other ports (Figure 1).
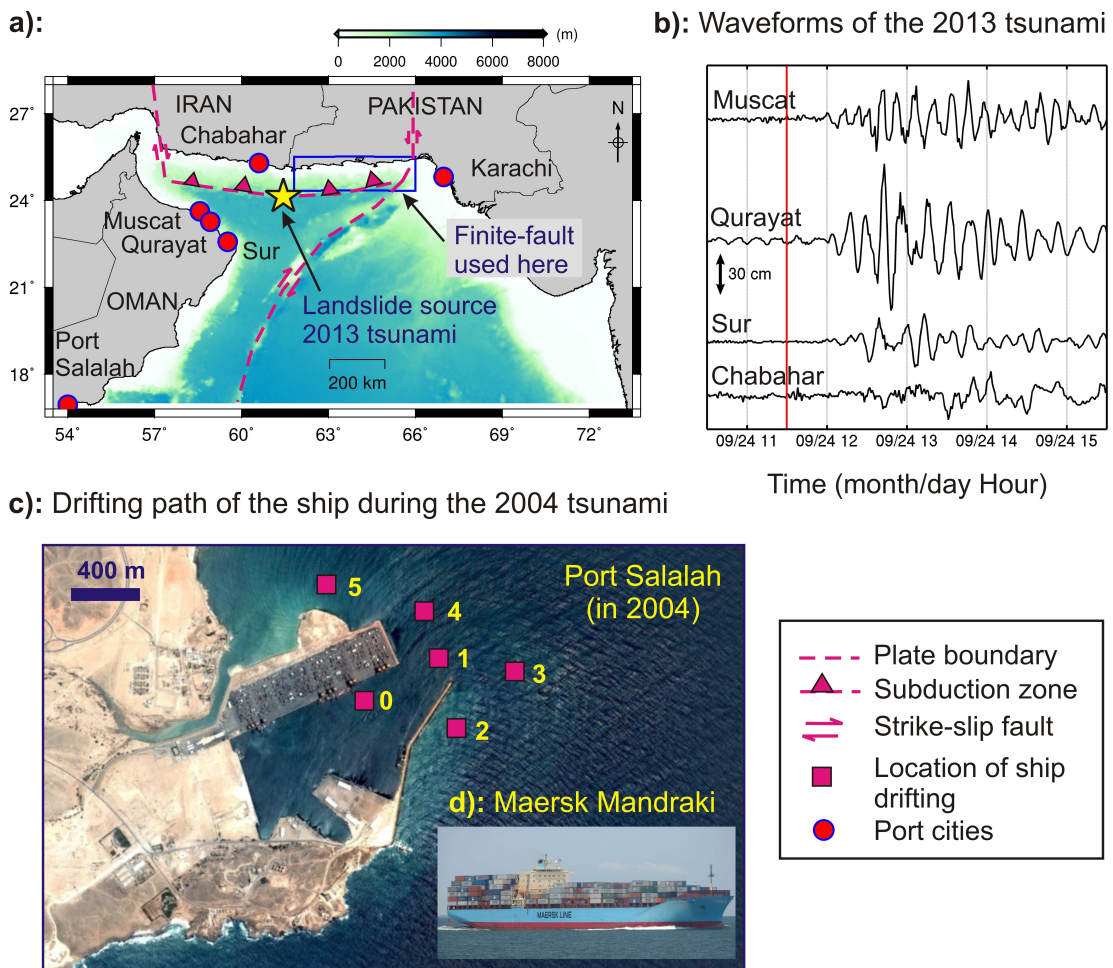

63

Figure 1: a) The Makran subduction zone area showing Karachi port studied in this work. b) Waveforms of the tsunami generated by a submarine landslide in the Makran region on 24 September 2013 based on Heidarzadeh and Satake (2014, Figure 11). c) Drifting of a large ship, the *Mearsk Mandraki* (shown in panel d) within the port of Salalah (pink squares) following the December 2004 Indian Ocean tsunami based on the data by Okal et al. (2006). The numbers to the right of each point indicate the sequence in which the ship drifted. d) The ship *Mearsk Mandraki* which was drifting in port Salalah following the 2004 Indian Ocean tsunami.

71 Overall, the above case from the 2004 tsunami provides evidence of the treacherous nature of tsunami currents in

72 harbors. Although it may seem rational to associate high wave amplitudes with high velocities, the arresting feature is

73 that the strong currents continued for hours after the waves with maximum amplitude had arrived (nearly 9 *h* in Salalah).

74 This is all the more consequential since conventional tsunami warnings may be lifted after visibly perceptible signs

75 of the tsunami (*i.e.* vertical displacement) have disappeared, whereas the strong currents may manifest later on. In

76 the case of the 2013 Makran tsunami also, it is highly probable that the coastal geometry and local bathymetry were

77 responsible for long tsunami oscillations.

94 The Makran Subduction Zone (MSZ) has given rise to tsunamis in 1945 (Byrne et al., 1992; Heidarzadeh et al.,

95 2008) and 2013 (Heidarzadeh and Satake, 2014). Recent studies estimate the megathrust potential for the eastern

96 part of the MSZ (blue rectangle, Figure 1) to be M_w $8.8 - 9.0$ (Smith et al., 2013). Given the peculiarities observed

97 in Makran ports during the 2004 and 2013 tsunamis, there is a pressing need for a comprehensive quantification of

98 tsunami hazard, and associated uncertainties, especially port velocities. However, the accurate simulation of tsunami

99 currents at shallow depths requires accurate coastline definition, high resolution bathymetry, and highly refined meshes,

100 over enough time to capture the maximum. Thus, in this study we employ spatial resolutions of $10\,m$ for coastline,

101 $30\,m$ for bathymetry, and $10\,m$ for the computational mesh, locally in the vicinity of Karachi port (Pakistan), for a total

102 simulation time of 12 hours. The large number of runs, at such resolutions, needed for probabilistic hazard assessments

103 stretches the limit of current High-performance Computing facilities, even with the latest GPU (Graphics Processing

104 Unit) acceleration (Reguly et al., 2018). In terms of the seabed deformation given as input to the tsunami model, we

105 introduce here an earthquake source designed with segments of size $5\,km \times 5\,km$ with carefully constructed positive

106 slip kernels to preserve fidelity to both magnitude scaling (Blaser et al., 2010) and slip scaling relations (Allen and

107 Hayes, 2017). Second, the presence of a considerable sediment layer over the Makran Subduction Zone (MSZ) (up to

108 $2\,km$) demands incorporation of its influence on the deformation, since a remarkable amplification of up to $60\,\%$ can

109 be generated (Dutykh and Dias, 2010).

110 We select a probabilistic route in order to quantify uncertainties in future tsunamis due to the uncertain earthquake

111 source variations (see the full workflow in Figure 2). However, since the probability of large events is small, a compre-

112 hensive coverage of the Gutenberg-Richter relation requires a large number of runs for the diversity of plausible events

113 to be well represented across magnitudes and source location (in the thousands at minimum for a coarse quantification

114 and much more for realistic assessments). Due to the considerable computational complexity of each high-resolution

115 tsunami simulation of coastal tsunami currents, such a probabilistic endeavor can only be achieved by replacing the

116 numerical tsunami model by a statistical surrogate: the emulator. To our knowledge, this is the first time that emula-

117 tion has been marshalled to generate future earthquake-generated tsunami currents; it has been employed only once in

118 the past for currents, for a single source of landslide-generated tsunamis with huge benefits in terms of computational
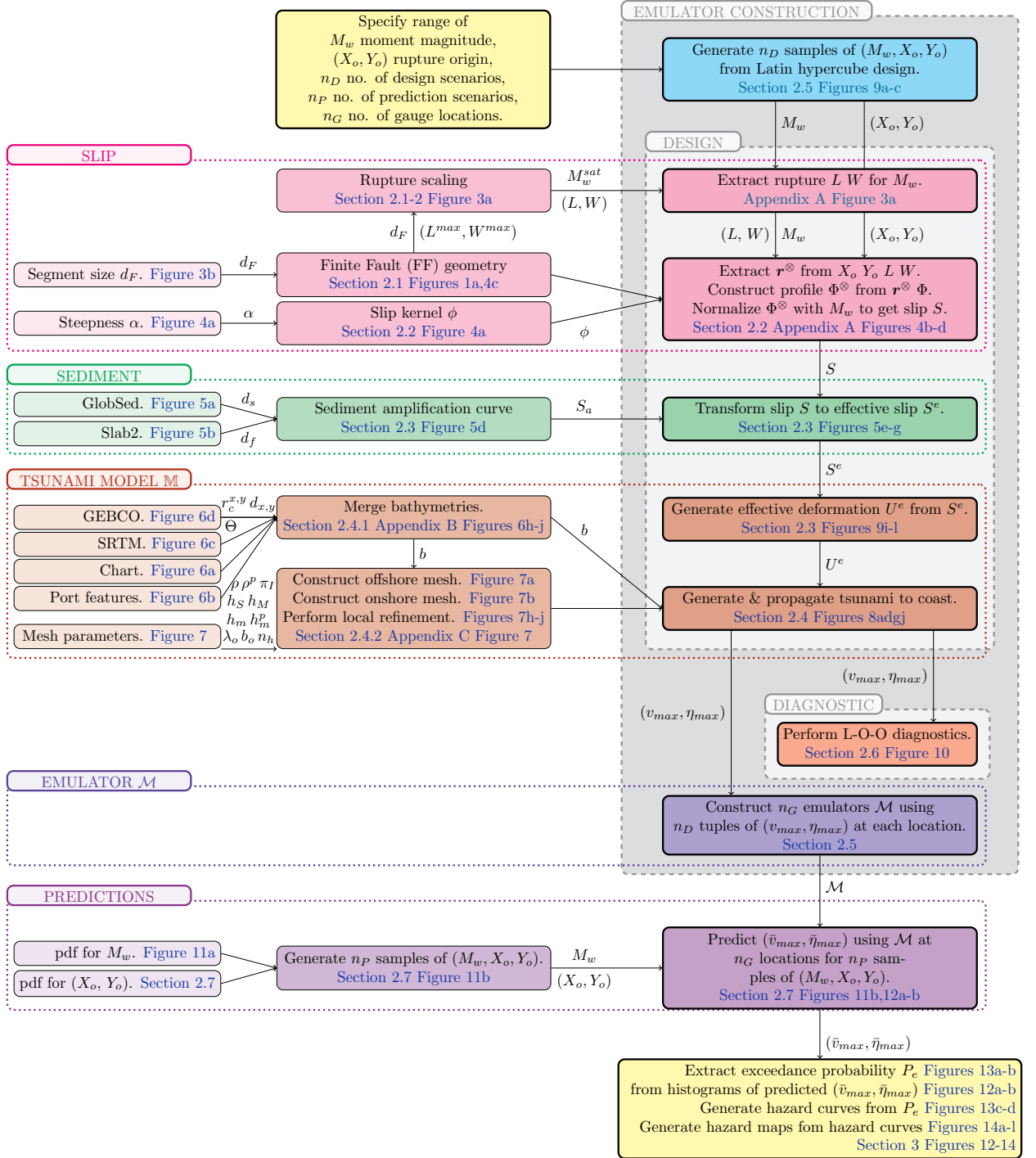
Figure 2: Global workflow describing the integration of different work components in this study for emulation-based probabilistic assessment of hazard for tsunami currents and heights in the port.

costs and hazard assessment (Salmanidou et al., 2019). With a design of only 300 runs, we fit an emulator to produce 1 million plausible tsunamis at any location. These emulated runs enable us to fully characterize uncertainty in future
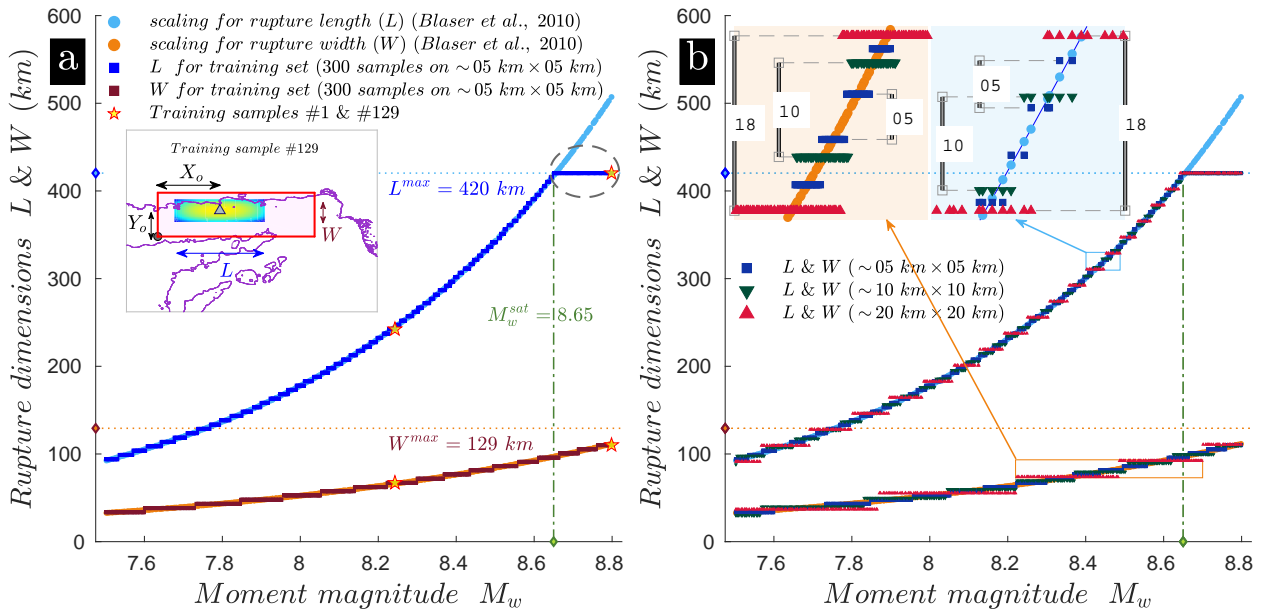
Figure 3: Finite fault model. a) Scaling relation of rupture length (L) and width (W) with respect to the rupture moment magnitude (M_w) showing the maximum length (L_{max}), width (W_{max}) and moment magnitude (M_w^{sat}) accommodable in the eastern MSZ. The lengths and widths of 300 earthquake scenarios are plotted over the scaling relation for an FF model made up of $\sim 5\,km \times 5\,km$ segments. The rupture length saturates after M_w 8.65 (green line) in the region marked by the ellipse. The inset plot display the rupture dimensions (L, W) and rupture origin co-ordinates (X_o, Y_o) on a sample scenario (no. 129). Sample nos. 1 and 129 are marked on the scaling curves. b) Same as (a) but also includes FF models made up of $\sim 5\,km \times 5\,km$, $\sim 10\,km \times 10\,km$ and $\sim 20\,km \times 20\,km$ segments. The inset plots zoom on to the scaling relation to reveal discontinuities in the realizable fault dimensions.
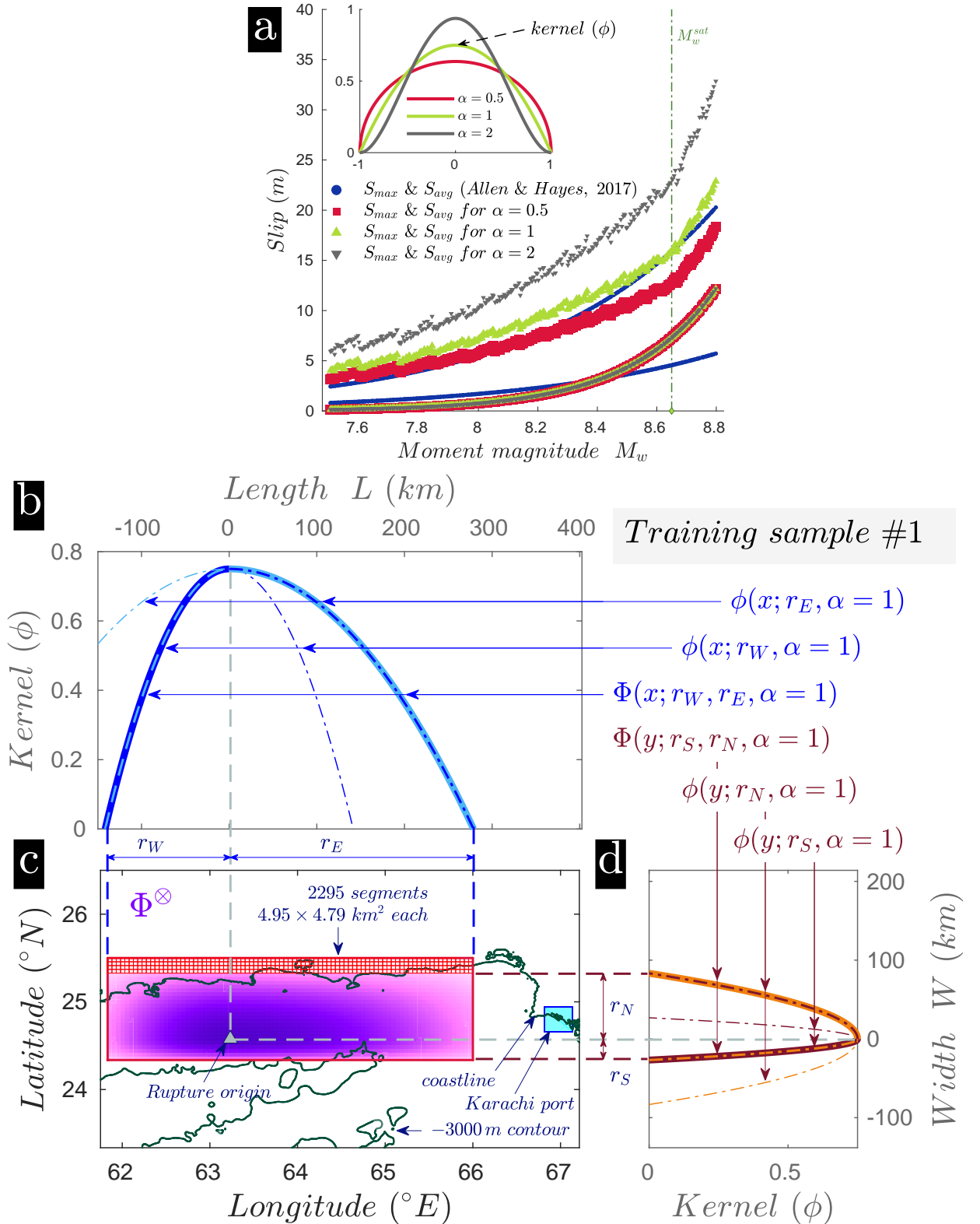
Figure 4: Slip profile generation. a) Validating maximum slips (S_{max}) and average slips (S_{avg}) for 300 earthquake scenarios as per the scaling relation in Allen and Hayes (2017) by varying the steepness (α) b) & d) Bi-lobed kernels $\Phi\left(x; r_E, r_W, \alpha\right)$ and $\Phi\left(y; r_S, r_N, \alpha\right)$ along fault length and width respectively for a sample scenario (no. 1). c) Tensor product $\Phi^\otimes$ of the two bi-lobed kernel functions in (b) and (d) prior to magnitude normalization.

121 tsunami currents. Section 2 describes the models and methods used in this work, Section 3 discusses the results, and

136 conclusions are drawn in Section 4.

2. Models, Data and Methods

138   In this section, we describe the finite fault apparatus (Section 2.1), construction of the slip profile on the finite

139 fault (Section 2.2), integration of the sediment amplification over the slips (Section 2.3), tsunami propagation (Section

140 2.4), merging of bathymetries at different resolutions (Section 2.4.1), design of algorithm for locally refined unstruc-

141 tured mesh (Section 2.4.2), emulator training (Section 2.5), emulator diagnostics (Section 2.6) and finally the hazard

142 predictions for 1 million events (Section 2.7). The global workflow is displayed in Figure 2.

143   There are formidable computational challenges that must be addressed in order to accurately represent both the

144 actual geophysical processes and their uncertainties. Often, in tsunami modeling this trade-off between capability and

145 capacity in High Performance Computing (HPC) is left unresolved by either radically simplifying the physics (*e.g.* a

146 linear tsunami propagation till say $100\,m$ depth with the use of an empirical relationship thereafter), or running only

147 a few high resolution simulations as scenarios. We argue that our tsunami emulation framework, in this context of

148 currents that are highly nonlinear and very sensitive to near shore bathymetry, provides a solution to this trade-off

149 between precision and coverage of uncertainties. It requires manipulation of very large data sets on HPC, as well as

150 complex post-processing on diverse software and data platforms. Thus, our work here is at the forefront of what can

151 be achieved using the most refined finite fault segmentation, the latest tsunami model acceleration schemes on GPU

152 clusters, hierarchical file formats, smart unstructured meshes and newest multi-threading emulation platforms.

2.1. Finite Fault Model

154   We construct a finite fault (FF) on the eastern section of MSZ (blue rectangle, Figure 1) using a total number

155 $\left(n_F\right)$ of 2295 rectangular segments (Figures 4c & 9j). The overall dimension of the FF model is $420\,km \times 129\,km$

156 ($L^{max} \times W^{max}$). The slip on a segment is denoted by S_i, where i varies from 1 to 2295. The closed-form equations from

157 Okada (1985) transform the slips and other FF parameters into a static vertical displacement denoted by U (calculated

158 inside an uplift calculation box, see Figures 9g & h). The final vertical displacement field results from the combined

159 superposition of vertical displacements due to all the activated fault segments. Among the FF parameters, the dip

160 angle and fault depth (d_f) are sourced from the recent plate boundary model, Slab2 (Hayes et al., 2018; Hayes, 2018).

161 The strike and rake angles are kept constant at 270° and 90°. Each segment size (d_F) is approximately $5\,km \times 5\,km$

162 ($l_i \times w_i$). All the segments are arrayed in an 85×27 grid. This resolution is chosen to preserve fidelity to the scaling

163 relation from Blaser et al. (2010) (Figure 3a), arrived through comparing the performance of different segment sizes

164 *viz.* $5\,km \times 5\,km$, $10\,km \times 10\,km$ and $20\,km \times 20\,km$ (Figure 3b). The discrepancy to the scaling relation appears as
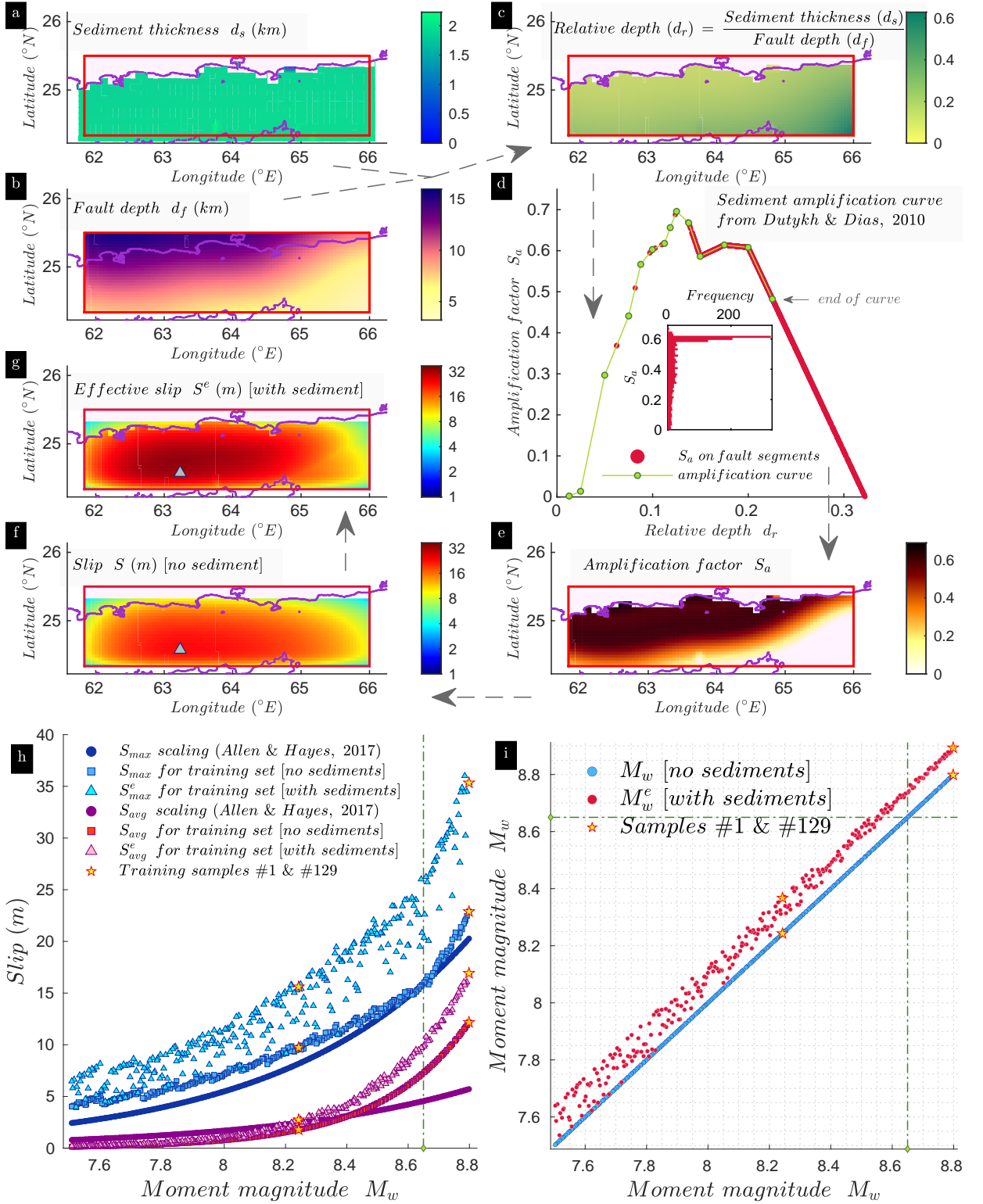
Figure 5: Sediment amplification. a) Sediment thickness d_s over eastern MSZ. b) Fault depth d_f. c) Relative depth d_r. d) Sediment amplification curve from Dutykh and Dias (2010). The inset histogram shows the distribution of S_a for all the FF segments. e) Sediment amplification factor S_a. f) Slip profile S without sediments. g) Effective slip profile S^e incorporating influence of sediments. h) Comparison of S_{avg} and S_{max} with and without the influence of sediments to slip scaling in Allen and Hayes (2017). i) Same as (h) but for moment magnitude with (M_w^e) and without (M_w) the effect of sediments.

165 discontinuities in the realizable fault lengths (L) and widths (W) (Figure 3a inset). The size of the discontinuities are

166 the same as the resolution chosen (Figure 3b inset). Thus, we observe the least discontinuity while using a $5\,km \times 5\,km$

167 segmentation (Figure 3). We use the definitions of the seismic moment M_w and moment magnitude M_0 (Kanamori,

168 1977; Hanks and Kanamori, 1979) as,

$$M_w = (2/3)\left(\log_{10} M_0 - 9.1\right), \qquad M_0 = \sum_{i=1}^{n_F} \mu l_i w_i S_i \tag{1}$$

170 with $\mu = 3 \times 10^{10}\,N/m^2$ being the modulus of rigidity. Our implementation of the Okada suite is adapted from the

171 dMODELS[1] code (Battaglia et al., 2012, 2013). The next section details the design of the slip profile over the FF

172 model.

2.2. Slip Profile Generation

174 Slips are usually modeled to be uniform on the FF segments, even though inversions of seismic sources evidenced

175 localised concentrations of high slips or asperities over a backdrop of lower slips (Grezio et al., 2017). To generate a

176 similar behaviour in our slip profiles, we utilize a positive kernel function ϕ having a functional form (Figure 4a inset):

177

$$\phi\left(x;r,\alpha\right) = \begin{cases} c_\alpha \left(1 - \left|\frac{x}{r}\right|^2\right)^\alpha & |x| \leq r \\ 0 & |x| > r \end{cases} \tag{2}$$

179 where $c_\alpha = \dfrac{\Gamma\left(2l+2\right)}{2^{2l+1}\Gamma\left(l+1\right)^2}$ is the normalizing constant made up of the gamma function (Γ), the length scale r defines

180 the domain where ϕ is non-zero and the parameter α adjusts the steepness of ϕ. Using ϕ as the core, we construct the

181 bi-lobed kernel function Φ:

$$\Phi\left(x;r_l,r_r,\alpha\right) = \begin{cases} \phi\left(x;r_l,\alpha\right) & -r_l \leq x \leq 0 \\ \phi\left(x;r_r,\alpha\right) & 0 \leq x \leq r_r \end{cases} \tag{3}$$

183 where r_l and r_r are the length scales of the left and right lobes of Φ, their values depending on the position of the rupture

184 origin (X_o, Y_o) with respect to the fault length (L) and width (W) (Figures 3a inset & 4b-d). The tensor product of the

185 two bi-lobed kernel functions, one along the length (Figure 4b) and another along the width (Figure 4d) of the fault

186 yields the surface $\Phi^\otimes$ (Figure 4c):

$$\Phi^\otimes\left(x,y;\boldsymbol{r}^\otimes,\alpha\right) = \Phi\left(x;r_W,r_E,\alpha\right) \otimes \Phi\left(y;r_S,r_N,\alpha\right) \quad (x,y) \in \left[-r_W,r_E\right] \times \left[-r_S,r_N\right] \tag{4}$$

[1] v1.0 available at *pubs.usgs.gov/tm/13/b1/*

188 where $\left[-r_W, r_E\right] \times \left[-r_S, r_N\right]$ denotes the domain of the rupture and $\mathbf{r}^\otimes = \left\{r_W, r_E, r_S, r_N\right\}$. A normalization of $\Phi^\otimes$

189 with the required moment magnitude on the rupture yields the final slip profile S (Figure 5f and 9e & f). The algorithm

190 for the above construction is detailed in Appendix A. Given the algorithm, we arrive at $\alpha = 1$ by varying α to closely

191 match the maximum slip S_{max} and average slip S_{avg} curves generated from the scaling relations in Allen and Hayes

192 (2017, Table 2) (Figure 4a). The next section describes the incorporation of the effect of seafloor sediment layer.

2.3. Sediment Amplification

194   Considerable amplification (up to 60 % locally) of crustal deformation due to the presence of layers of sediments

195 on the seafloor was shown in Dutykh and Dias (2010, Figure 12). We introduce it here in tsunami modeling, by making

196 use of the sediment amplification curve (Figure 5d). The curve uses the relative depth (d_r^i) of the ith segment (Figure

197 5c) calculated as:

198
$$d_r^i = \frac{d_s^i}{d_f^i} \tag{5}$$

199 where d_s^i is the sediment thickness over the segment interpolated from GlobSed[2] (Straume et al., 2019), and d_f^i is the

200 down-dip fault depth of the segment taken from Slab2 (Hayes et al., 2018) (Figures 5a & b). Given d_r^i, the sediment

201 amplification curve supplies the sediment amplification factor (S_a^i) on the segment (Figure 5e). The amplification

202 due to the sediments is incorporated by multiplying the slip S^i (Figure 5f) with the sediment amplification factor S_a^i

203 resulting in an effective slip S_i^e (Figure 5g):

204
$$S_i^e = S_i \left(1 + S_a^i\right) \tag{6}$$

205 The closed-form equations from Okada (1985) transform the effective slips S_i^e into the effective vertical displacement

206 U^e (Figures 9k & l). The influence of sediments not only increases the slips but also modifies the profile, as evident

207 in the emergence of a double-lobed profile in the effective slip (Figure 5g). The effect is more conspicuous in the

208 associated deformations (compare Figures 9g & k). The amplification factor (S_a) peaks at a relative depth of approx-

209 imately 0.13 after which it decreases. Given the geometry of the fault and overlying sediment profile, a significant

210 number of segments have an amplification factor between $0.4 - 0.6$ (or, equivalently a $40 - 60$ % amplification) (Fig-

211 ures 5d inset & e). Furthermore, the sediment amplification factor for the whole MSZ is shown in Figure 5e; its value

212 is strongly dominated by the fault depth (Figure 5b) rather than the sediment thickness (Figure 5a) which is uniform

213 around 2 km. The sediment amplification curve is defined only till a relative depth of 0.23 in Dutykh and Dias (2010).

214 We linearly extrapolate the curve in order to be as conservative as possible in the region where it is not defined as

---

[2]available from *ngdc.noaa.gov/mgg/sedthick/*

215 well as to smoothly transition from regions of higher to lower fault depths. The counterparts of average slip S_{avg} and

216 maximum slip S_{max} of S (without sediments) are defined as average effective slip S_{avg}^e and maximum effective slip

217 S_{max}^e of S^e (with sediments). Similarly, effective moment magnitude M_w^e is defined, by replacing S_i with S_i^e in Eqn.

218 1. The effect of sediments on slips is compared in Figure 5h. Here, the increased scatter of S_{max}^e compared to S_{avg}^e

219 is due to the spatial distribution of S_a, which significantly amplifies S_{max}^e depending on the rupture origin (X_o, Y_o).

220 Also, the increase in scatter of S_{max}^e as M_w decreases is due to the decrease in rupture dimensions that allow many

221 earthquake scenarios to be situated in areas of lower S_a. This aspect is pronounced in a similar comparison of M_w^e to

222 M_w in Figure 5i. The next section describes the propagation of the tsunami resulting from the deformations caused

223 by the effective slips.

## 233 2.4. Tsunami Propagation

234 Unlike simulations for analysing wave heights which require a few hours of simulation time, capturing the veloci-

235 ties need a longer simulation time. Thus, each scenario is run for 12 h of simulation time (T_s) to obtain the maximum

236 tsunami velocity and wave height, and therefore is computationally expensive. It is not only imperative that the numer-

237 ical algorithms in the computer code for tsunami simulations run efficiently at fine mesh resolutions needed to capture

238 the currents (10 m), but also that the code is amenable to adequate parallelisation. Thus, to run 300 such scenarios, we

239 employ VOLNA-OP2[3] that has been shown to run efficiently for unstructured meshes on parallel GPUs (Reguly et al.,

240 2018). The number of scenarios (*i.e.* 300) is considerably higher than in existing studies (Rashidi et al., 2020; Hasan

241 et al., 2017; Heidarzadeh and Kijko, 2011). Usual simulations employ the Green's functions approach to superpose the

242 tsunami wave heights due to a multi-segment finite fault source. Here, we use the the Non-linear Shallow Water Equa-

243 tions (NSWEs) to model not only the propagation of the tsunami but also the run-up/down processs at the coast (Dias

244 et al., 2014). The finite volume (FV) cell-centered method for tessellation of control volume is used in VOLNA. Thus,

245 the barycentres of the cells are associated with the degrees of freedom. Dutykh et al. (2011) and Giles et al. (2020)

246 may be referred for details of numerical implementation, validation against standard benchmarks and comprehensive

247 error analysis. VOLNA models the tsunami life-cycle with:

248
$$\frac{\delta H}{\delta t} + \nabla \cdot (H\boldsymbol{v}) = 0 \tag{7}$$

249

250
$$\frac{\delta H\boldsymbol{v}}{\delta t} + \nabla \cdot \left(H\boldsymbol{v} \otimes \boldsymbol{v} + \frac{g}{2} H^2 \mathbf{I}_2 \right) = gH\nabla b \tag{8}$$

---

[3]v1.5 available at *github.com/reguly/volna*, with improvements to second order FV scheme and boundary conditions
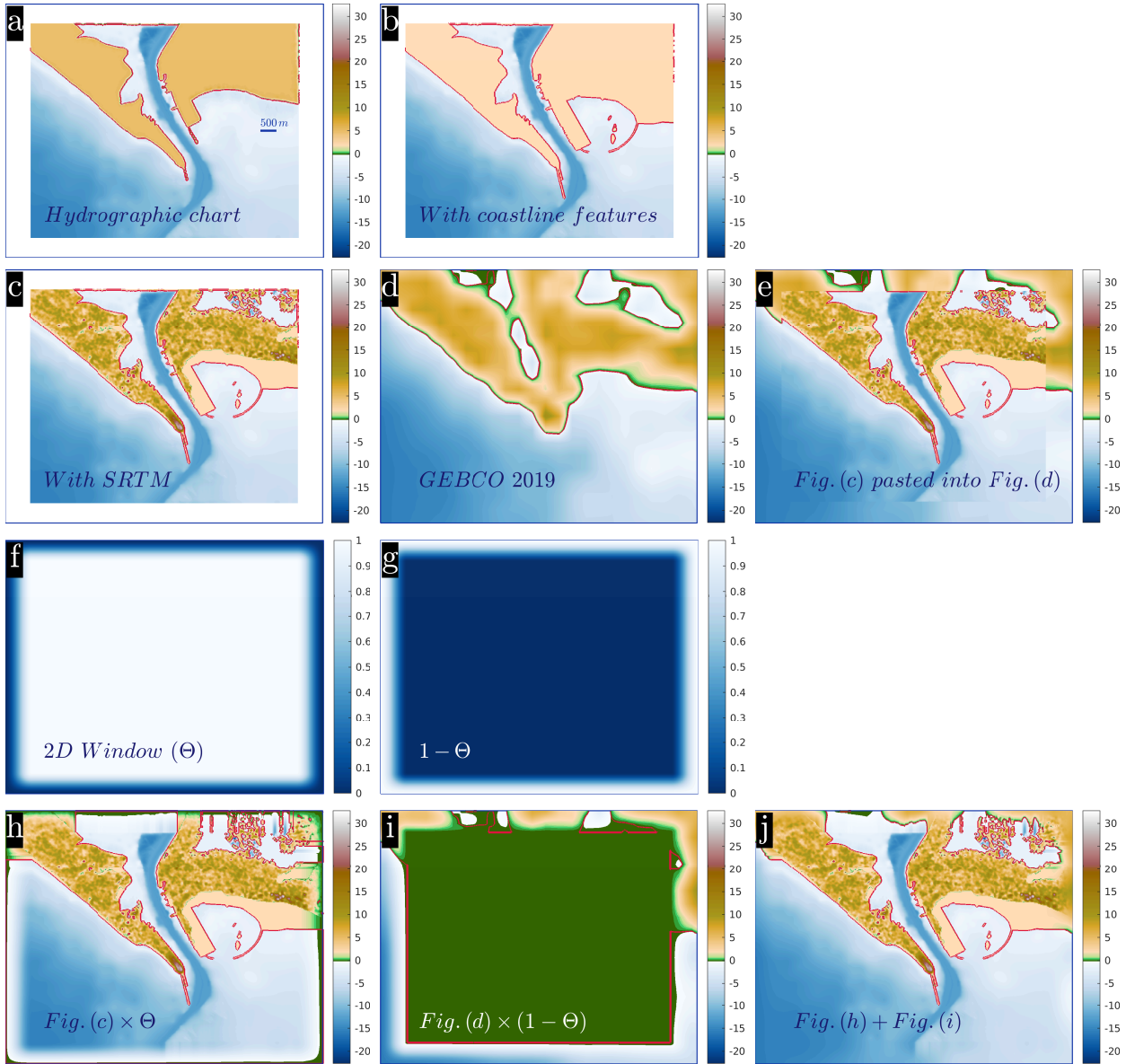
Figure 6: Merging of bathymetries. a) Digitized hydrographic chart bathymetry around Karachi port. b) Chart data with altered coastline after addition of port features from Google Earth. c) Chart data supplemented with SRTM data. d) GEBCO bathymetry around Karachi port. e) Merged bathymetry with chart data in (c) pasted into GEBCO bathymetry in (d). f) 2D window (Θ). g) Complement of Θ, *i.e.* $(1-\Theta)$. h) Chart bathymetry in (c) muliplied by window. i) GEBCO bathymetry in (d) multiplied by complement of window. j) Final merged bathymetry resulting from addition of windowed bathymetries in (h) and (i).

where $H(\boldsymbol{x}, t) = b + \eta$ is the total water depth defined as the sum of free surface elevation $\eta(\boldsymbol{x}, t)$, and time-dependent bathymetry $b(\boldsymbol{x}, t)$. The two horizontal components of the depth-averaged fluid velocity are contained in $\boldsymbol{v}(\boldsymbol{x}, t)$, g is the standard gravity and $\mathbf{I}_2$ is the 2×2 identity matrix. The maximum tsunami velocity v_{max} and wave height η_{max} at

264 a location $(\boldsymbol{x}, t)$ are computed as:

255
265
$$v_{max}(\boldsymbol{x}) = \max_{0 < t \leq T_s} \|\boldsymbol{v}(\boldsymbol{x}, t)\|_2 \tag{9}$$

266

267
$$\eta_{max}(\boldsymbol{x}) = \max_{0 < t \leq T_s} \eta(\boldsymbol{x}, t) \tag{10}$$

268 The dynamic bathymetry $b(\boldsymbol{x}, t)$ is composed as:

269
$$b(\boldsymbol{x}, t) = b_s(\boldsymbol{x}) + U^e(\boldsymbol{x}, t) \tag{11}$$

270 where b_s is the static bathymetry and U^e is the effective deformation due to the influence of sediments (Section 2.3). In

271 this work, an instantaneous rupture is assumed, *i.e.* U^e is supplied once at the beginning of the simulation. Further, to

272 reduce the computational burden of calculating deformations from 300 ruptures, U^e is computed only within a uplift

273 calculation box covering the rupture (see green rectangle in Figures 9g-h & k-l). We now move on the bathymetry

274 b_s and unstructured mesh, both vital components for an accurate modeling of currents in shallow water and near the

275 coast.

2.4.1. Merging of Bathymetries

277 The bathymetry used for the simulations is sourced from the GEBCO 2019 data set (GEBCO Bathymetric Com-

278 pilation Group 2019, 2019), having a resolution of 15″ (Figure 6d). Accurate modeling of port velocities and currents

279 near the coast requires high resolution bathymetry and good definition of the coastline. Towards this, we use digitized

280 bathymetry data at a resolution of $\sim 30\,m$ from hydrographic charts for Karachi port (Figure 6a). Further, we correct

281 the shoreline using satellite imagery from Google Earth at $\sim 10\,m$ resolution wherever port structures and breakwaters

282 need to be resolved (Figure 6b). The charts do not contain topographic data, which we supplement with SRTM v3[4] 1″

283 data (Figure 6c). Simply replacing the GEBCO data with the hydrographic chart data gives rise to sharp and unrealistic

284 discontinuities in the merged data set (Figure 6e). We ameliorate this by smoothly merging the hydrographic data into

285 the GEBCO data by a procedure using cosine-tapered Tukey windows (Figures 6f-g). The detailed algorithm can be

286 found in Appendix B.

2.4.2. Localised Non-Uniform Unstructured Mesh

294 We design a customised mesh algorithm for the unstructured mesh sizing function in three stages corresponding to

295 offshore, onshore and port regions. A strategy based on bathymetry $b(\boldsymbol{x})$ is used to generate the mesh in sea (Figure 7a),
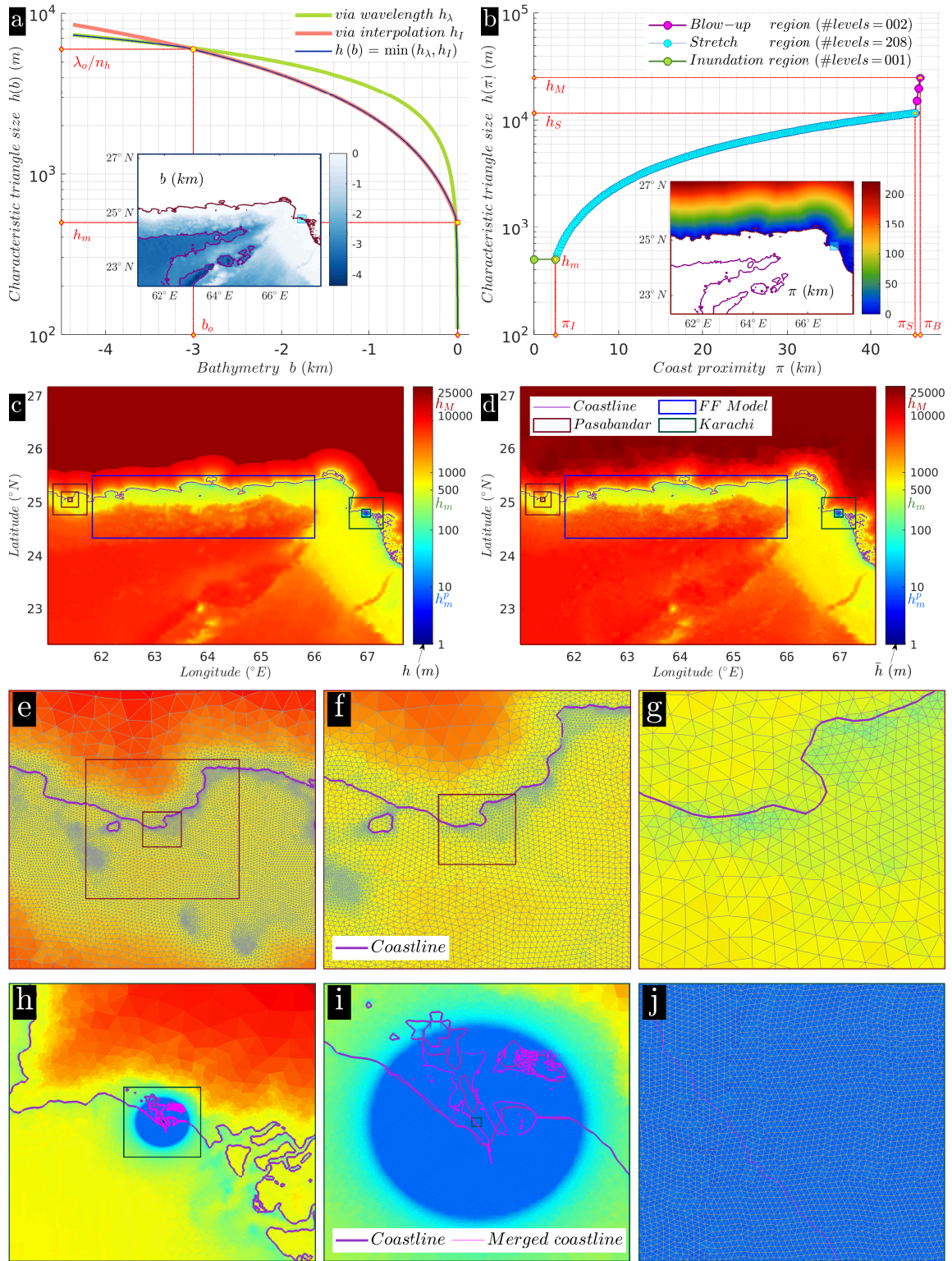

[4]available from *earthexplorer.usgs.gov*

Figure 7: Localised non-uniform unstructured mesh. a) Mesh-sizing rule for offshore mesh based on bathymetry b, shown in the inset. b) Mesh-sizing rule for onshore mesh based on coast proximity π, shown in the inset. c) Mesh sizing function h supplied to Gmsh for the whole domain resulting from the mesh-sizing rules in (a) and (b). d) Actual mesh sizes $\bar{h}$ in mesh generated from Gmsh using the mesh sizing function in (c). e-g) [*no local refinement*] Mesh at Pasabandar shown at scales of $64\,km \times 64\,km$, $32\,km \times 32\,km$ and $8\,km \times 8\,km$ respectively. h-j) [*with local refinement*] Mesh at Karachi port shown at scales of $64\,km \times 64\,km$, $16\,km \times 16\,km$ and $0.5\,km \times 0.5\,km$ respectively.
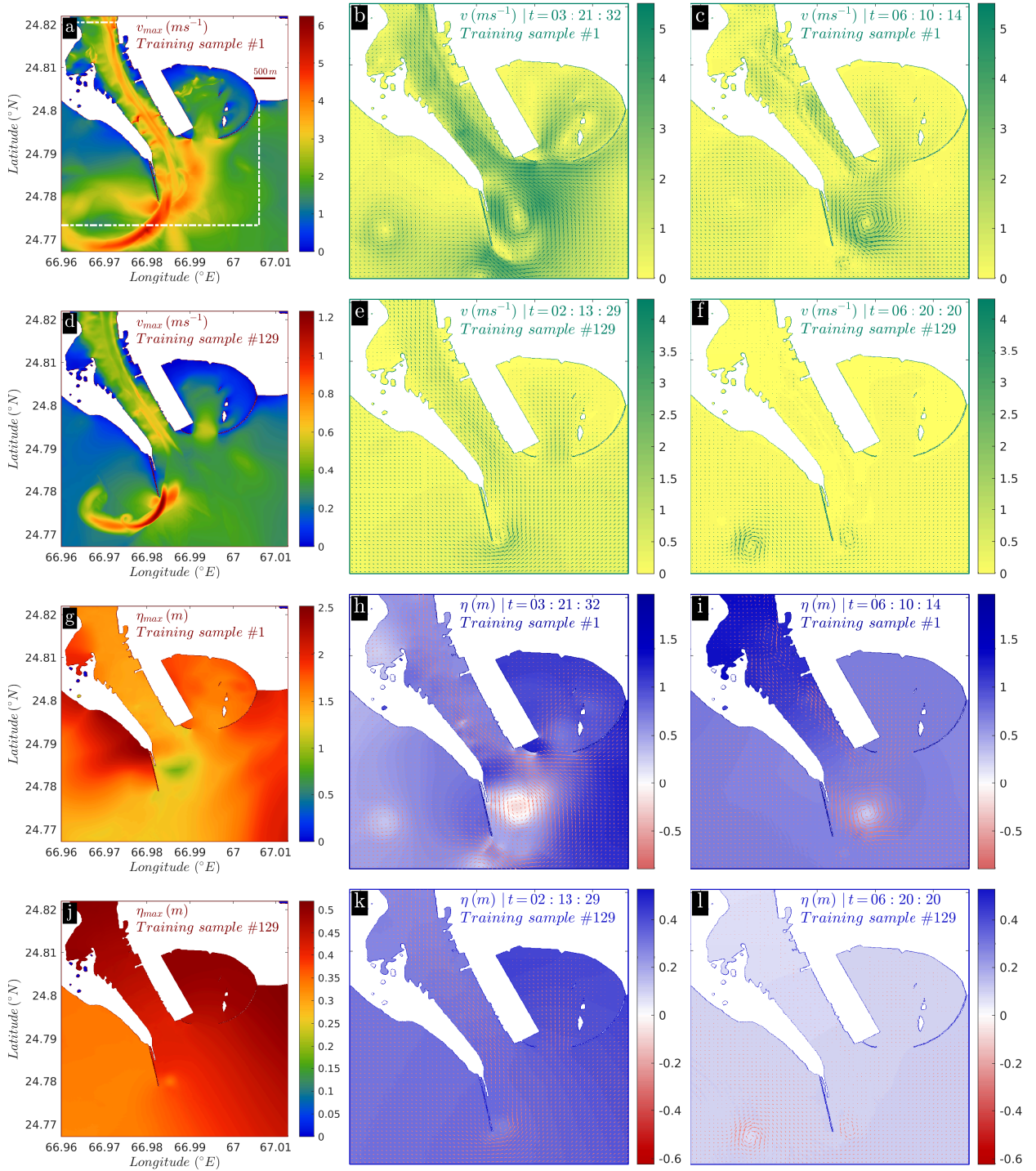
Figure 8: Tsunami propagation. a) Maximum velocity v_{max} around Karachi port over a simulation time of $12\,h$ for sample no. 1. b-c) Snapshots of velocities v for sample no. 1 at various times restricted to the box (dashed line) in (a). d-f) Same as (a-c) but for sample no. 129. g-l) Same as (a-f) but for tsunami height η_{max} (and η).
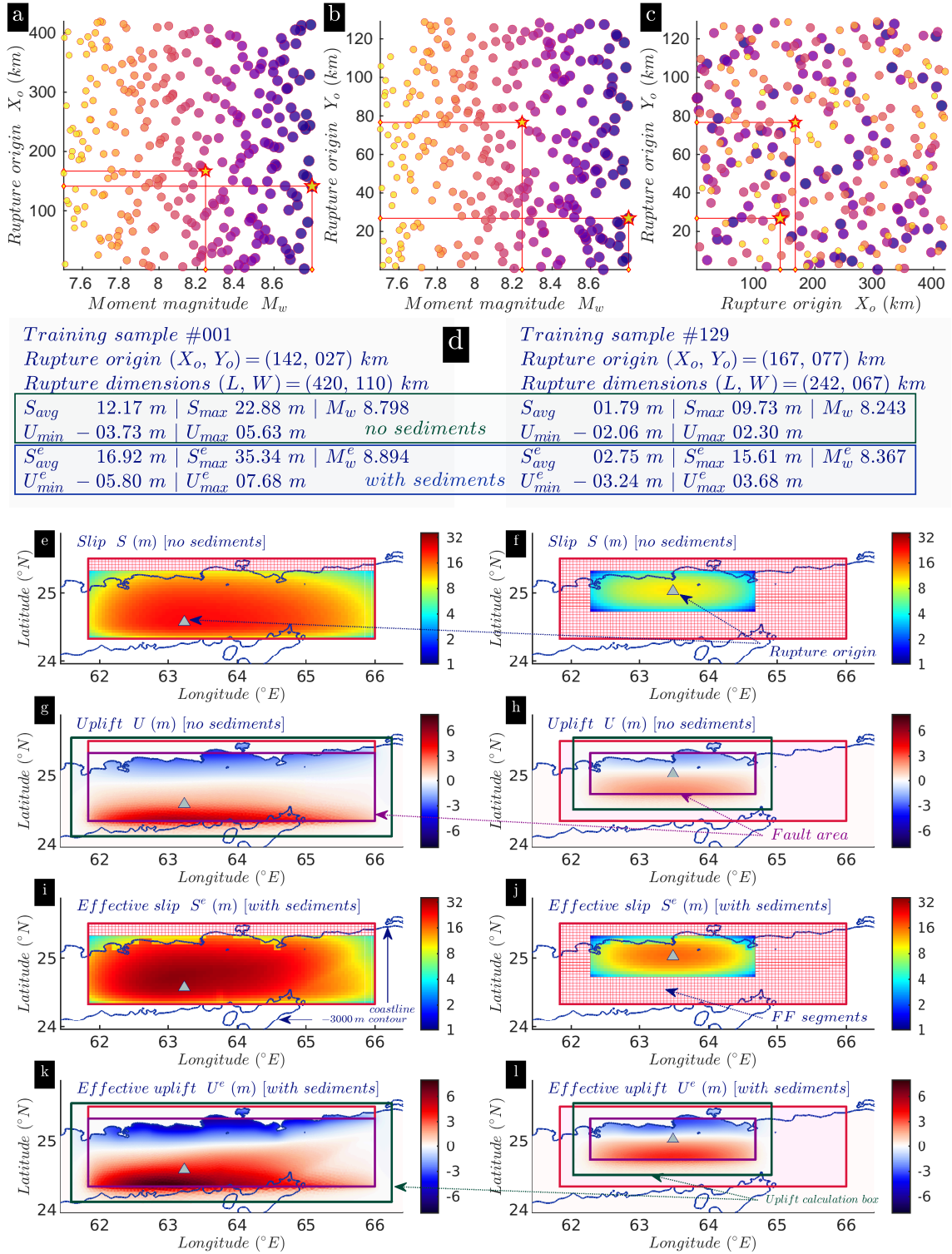
Figure 9: Training set of 300 scenarios of $\left(M_w, X_o, Y_o\right)$ generated by Latin Hypercube Design. a) Training set projected on $M_w - X_o$ plane. Sample nos. 1 and 129 are marked with stars. b) Same as (a) but on $M_w - Y_o$ plane. c) Same as (a) but on $X_o - Y_o$ plane. d) Comparison of relevant quantities for sample nos. 1 and 129. e) Slip S for sample no. 1 before incorporation of sediment influence, plotted on log_2 scale. f) Same as (e) but for sample no. 129. g) Offshore deformation U due to slip S for sample no. 1. h) Same as (g) but for sample no. 129. i) Effective slip S^e for sample no. 1 after incorporation of sediment influence. j) Same as (i) but for sample no. 129. k) Effective deformation U^e due to slip S^e for sample no. 1. l) Same as (k) but for sample no. 129.

296 whilst proximity to the coast $\pi(x)$ is used to size the mesh on land (Figure 7b). We also locally refine the mesh to 10 m

297 resolution at Karachi port (Figure 7h-j). This three pronged strategy strikes a balance between the fine mesh resolution

298 required near the port for resolution of velocities and associated overall computational cost. The non-uniform meshes

299 for the simulation are generated using Gmsh[5] (Geuzaine and Remacle, 2009). Considering the dimensions of the finite

300 fault earthquake sources ($L \times W$), we assume an approximate source wavelength ($\lambda_o < \sqrt{L^2 + W^2}$) of the tsunami,

301 and a representative ocean depth of the Makran trench ($b_o \sim 3\,km$), and calculate the time period (T_λ) of the wave as,

302
321
$$T_\lambda = \lambda_o / \sqrt{g b_o} \tag{12}$$

322 Here, $\lambda_o = 60\,km$, which is around 60 % of the maximum distance contained in the smallest rupture considered in this

323 work, i.e. of size $\sim 94\,km \times 34\,km$ for a M_w 7.5 event (sample no. 300). Next, assuming that the time period of the

324 tsunami is the same everywhere in the domain, we get for a depth $b(x)$ (van Scheltinga et al., 2012),

325
$$\lambda_n / \sqrt{b(x)} = \lambda_o / \sqrt{b_o} \tag{13}$$

326 which in turn relates the characteristic triangle (or element) length $h_\lambda(b)$ for depth $b(x)$ as,

327
$$h_\lambda(b) = \left(\lambda_o / n_h \right) \sqrt{b(x) / b_o} \tag{14}$$

328 where $n_h = \lambda_n / h_\lambda(b) = 10$ is the number of triangles in one wavelength λ_n. At the shore (i.e. $b = 0$), a minimum mesh

329 size h_m of 500 m is specified. In the vicinity of the port, the mesh size h_m^p is fixed as 10 m. We also fix the maximum

330 triangle size (h_M) as 25 km for regions that are deep inland. Further details and construction process for onshore and

331 port mesh sizing functions are elaborated in Appendix C. After feeding the mesh sizing function (Figure 7c) into Gmsh,

332 we get the computational mesh with ~ 2.64 million cells or triangles (Figure 7d). Figures 7e-g & h-j show enlarged

333 pictures of the mesh at increasingly fine scales for regions with (Pasabandar port) and without (Karachi port) local

334 refinement respectively.

335   The outputs v_{max} and η_{max} for two training samples, no. 1 and 129 are plotted in Figure 8. The figures also contains

336 snapshots taken at various time instants during the simulation.

2.5. Emulator Construction

338   The numerical simulation of the tsunami life cycle, i.e. its generation, propagation and inundation at fine mesh

339 resolutions is computationally expensive due to non-linearity, and typically consumes hours on supercomputers. This

340 is all the more prohibitive for a probabilistic quantification since thousands of runs of the forward model are required

341 to adequately capture the various plausible scenarios. Statistical surrogates (or emulators) provide a computationally

---

[5]v4.4.1 available at *gmsh.info*
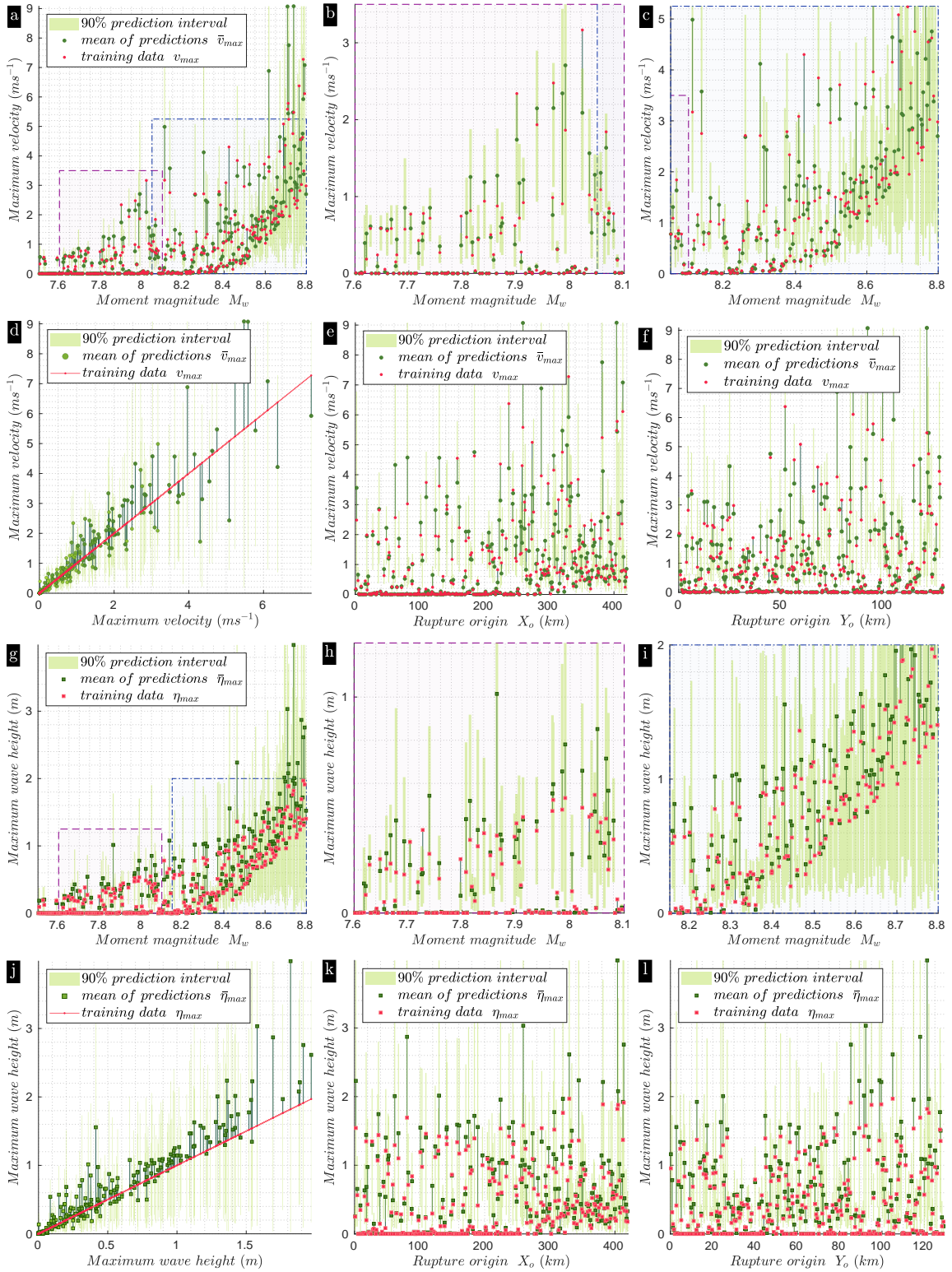
Figure 10: Emulator diagnostics. a) L-O-O for emulation of maximum velocity v_{max} at a gauge in Karachi port (gauge no. 91 in Figures 12a-b). The vertical line segments connect the training data to its predicted counterpart. b) Enlargement of lower moment magnitude region in (a). c) Enlargement of higher moment magnitude region in (a). d) Same data in (a) plotted to show trend of predicted $\bar{v}_{max}$ with respect to training v_{max}. e) Same data in (a) but plotted with respect to x-coordinate of rupture origin X_o. f) Same data in (a) but plotted with respect to y-coordinate of rupture origin Y_o. g-l) Same as (a)-(f) but L-O-O for emulation of maximum height η_{max} at gauge no. 91.

342 cheap approximation of the complex tsunami solvers, together with estimates of uncertainties in these predictions. In

343 this study, the three input model parameters are moment magnitude (M_w) and rupture origin co-ordinates (X_o, Y_o)

344 (Figure 3 inset). The inputs are transformed into effective seafloor displacements (Sections 2.1, 2.2 & 2.3). The

345 consequent tsunamis are propagated till Karachi port (Section 2.4). The outputs of interest in our case are the maximum

346 wave height (η_{max}) and maximum wave velocity (v_{max}) at n_G (193) virtual gauge locations around the port.

347 Thus, the computer code (denoted by $\mathbb{M}$) simulates a multi-physics two-stage physical model, *i.e.* from slips S^e

348 to deformation U^e, then from U^e to tsunami outputs v and η. A design of computer experiments is an essential stage

349 to create the data set used to construct the emulator. This consists of evaluations of the model (or computer runs

350 of $\mathbb{M}$) at a finite number of locations in the space of input model parameters, together called the training set. We

351 employ a Latin Hypercube Design (LHD) of size 300 for 3 parameters (Figures 9a-c). This is large enough to capture

352 complex nonlinear combined sensitivities to the input parameters (*e.g.*, the influence of size and location in small and

353 mid-size events closer to Karachi, or large regional variations in spatial distributions of slips), but still fits within our

354 computational budget. The Gaussian Process (GP) emulator (denoted by $\mathcal{M}$) interpolates across the input-output points

355 in the training set, and generates uncertain predictions elsewhere in the space of input parameters. The uncertainty

356 in the predictions is modeled by a normal distribution whose mean and standard deviation are calculated using the

357 Kriging formula (mean quantities denoted by $\bar{v}_{max}$ and $\bar{\eta}_{max}$). Derivations and exact equations can be found in Section

358 2 of Beck and Guillas (2016, Eqn. 2.4). GP emulation has been instrumental in successfully quantifying uncertainties

359 in tsunami heights generated by landslides over the North Atlantic and the Western Indian Ocean as well as earthquakes

360 over Cascadia (Salmanidou et al., 2017; Guillas et al., 2018; Salmanidou et al., 2019).

361 Maximum velocity magnitudes (and heights) are positive. In order to respect this physical constraint and not predict

362 negative velocities (and heights), we feed the logarithm of v_{max} (and η_{max}) into the construction of the emulator. Since

363 the constructed emulator is now in the logarithmic scale, we transform the predicted quantities back to the original

364 scale by accounting for the lognormal nature of the predicted distributions. Hence, the confidence intervals for the

365 predictions, representing uncertainties, are all rendered positive, and naturally skewed in that direction, see Figure 10.

366 Once the emulator is constructed, it needs to be validated before employing it for predictions. We turn to this aspect

367 in the next section.

368 ## 2.6. Emulator Diagnostics

369 In order to validate the quality of the emulation, we provide Leave-one-out (L-O-O) diagnostics here. As described

370 in Section 2.5, our training set consists of 300 pairs of input-output quantities. In L-O-O, a reduced training set of 299

371 pairs is employed to build an emulator, which is then used to predict the output at inputs in the 1 pair that was left

372 out. The predicted output (and its uncertainty) is compared to the actual output in the left out pair. This procedure

373 is repeated 300 times to cover all the pairs in the training set. These tests are passed by the emulator, as seen for

374 predicted $\bar{v}_{max}$ in Figures 10a-f and $\bar{\eta}_{max}$ in Figures 10g-l. The comparison between the mean of predictions from

375 the emulator $\mathcal{M}$ and the training data from the tsunami simulator $\mathbb{M}$ shows that the emulator approximates well the

376 simulator. The vertical line segments connects the predicted means with the counterpart in the training data. More

377 importantly, the uncertainties in the predicted mean, quantified in the form of 90% prediction intervals (green bars in

378 Figure 10), represent well the uncertainties about these predictions (or are even slightly conservative) since around

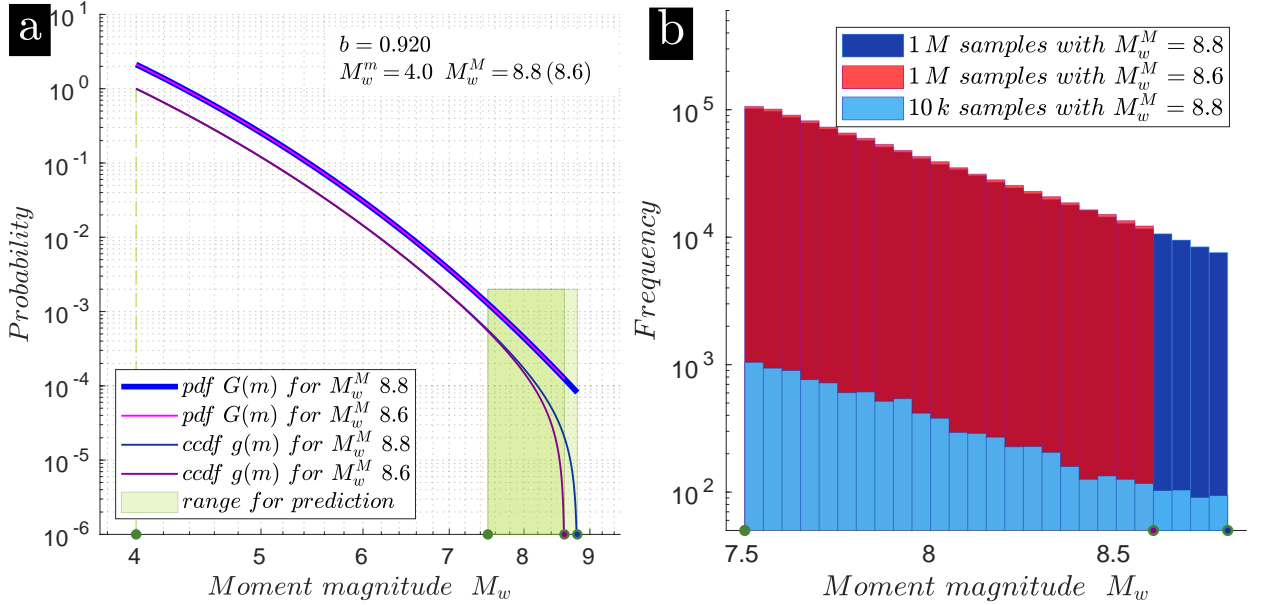379 90% or more of the outputs from the training set fall within these intervals.

382 **Figure 11:** Emulator predictions. a) The Gutenberg-Richter (G-R) relation for the MSZ, showing probability and com-
383 plementary cumulative distribution functions for two maximum moment magnitude assumptions, *viz.* 8.6 and 8.8. b)
384 Histograms of 1 million (and 10,000) samples of M_w used as inputs for predictions.

2.7. Emulator Predictions

405   Although the 300 simulations by itself may be considered to generate a good description of the hazard, a large

406 number of scenarios are essential for a comprehensive probabilistic hazard assessment. Thus, we evaluate the model at

407 n_P (1 million) values of $\left(M_w, X_o, Y_o\right)$ at 193 virtual offshore gauges (locations shown in Figure 12). The constructed

408 emulator is used to evaluate the model at inputs that are different from those in the training set. These evaluations are

409 termed predictions. A prediction returns the mean value of the emulated quantity and a measure of inherent statistical

410 error/uncertainty in the approximation, *e.g.* the standard deviation. Cumulatively, these 193 million predictions not

411 only comprehensively cover the geography around Karachi port, but also exhaustively sweep through the entire range

412 of events in the magnitude-frequency distribution. Additionally, such a high number of samples is also needed to
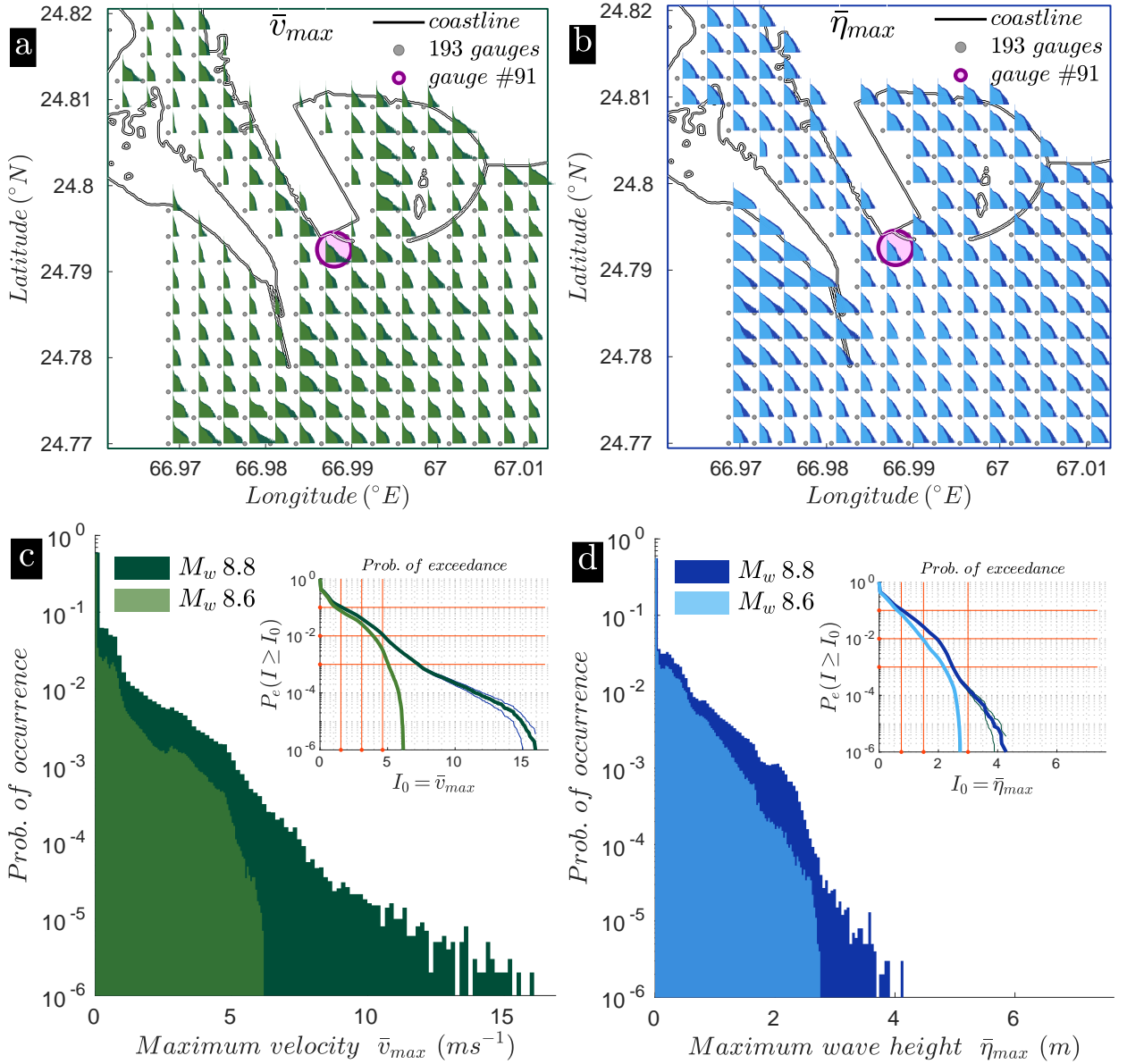
386
387
388 **Figure 12:** Raw output from 1 million predictions at 193 gauges. a) Histograms of 1 million predicted maximum velocities
389 $\bar{v}_{max}$ at each of the 193 gauges. Each histogram has the same scale as (c). Histograms from maximum moment magnitude
390 of 8.8 and 8.6 are superimposed. b) Same as (a) but for predicted maximum heights $\bar{\eta}_{max}$. c) Enlarged normalized
394
391 histograms of predicted maximum velocities at gauge no. 91 comparing the two cases of different maximum moment
392 magnitude. Inset shows probability of exceedance curves extracted from the histograms, with 99 % confidence interval. d)
393 Same as (c) but for predicted maximum heights.

413 thoroughly explore the interplay among the three parameters in the input space of $\left(M_w, X_o, Y_o\right)$.

414 The 1 million M_w values are sampled from the Gutenberg-Richter (G-R) distribution for the MSZ. Here, the probability

415 distribution function (pdf) for the G-R relation is modeled as the doubly truncated exponential distribution (Cosentino
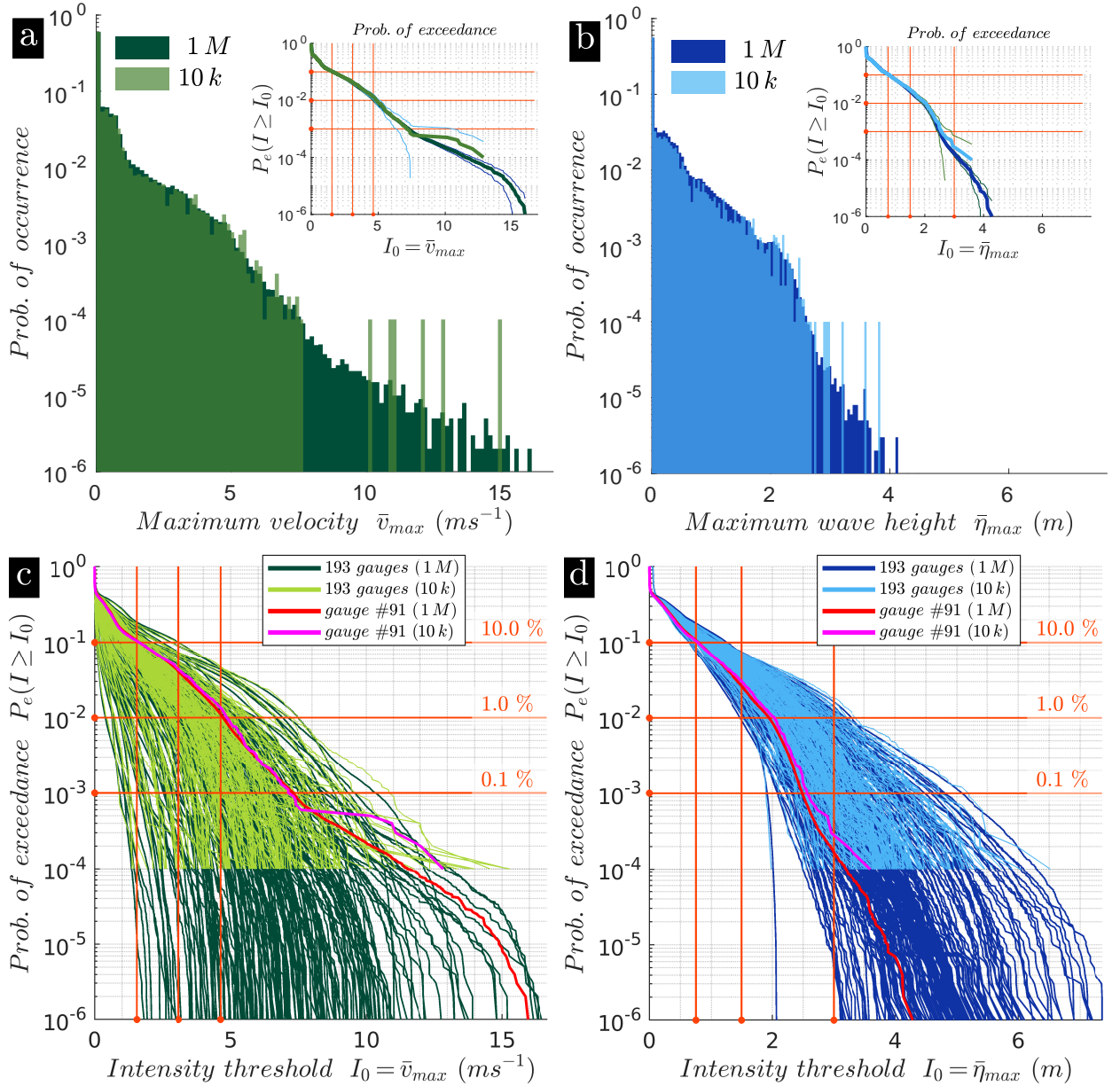
Figure 13: Hazard curves. a) Comparison of normalized histograms of 1 million and 10,000 predicted maximum velocities $\bar{v}_{max}$ at gauge no. 91. Inset shows probability of exceedance curves extracted from the histograms, with 99 % confidence intervals. b) Same as (a) but for predicted maximum heights $\bar{\eta}_{max}$. c) Probability of exceedance curves for predicted maximum velocities at 193 gauges. The curves for 10,000 predictions are superimposed over those from 1 million predictions. Curves for gauge no. 91 are marked out. Chosen values of probabilities and intensity thresholds used to generate hazard maps are marked as horizontal and vertical lines respectively. d) Same as (c) but for predicted maximum wave heights.

et al., 1977):

$$
G(m) = \begin{cases} \dfrac{\beta e^{-\beta(m - M_w^m)}}{1 - e^{-\beta(M_w^M - M_w^m)}} & M_w^m \leq m \leq M_w^M \\ 0 & m > M_w^M \end{cases} \tag{15}
$$

418   where $\beta = b \log_e 10$ and the lower M_w^m and upper M_w^M limits of truncation are 4 are 8.8 respectively. This rate parameter

419   b of 0.92 specific to the MSZ is taken from the most recent Earthquake Model of Middle East (EMME) database

420   (Danciu et al., 2018, Table S1). The complementary cumulative distribution function (ccdf), also called probability of

421   exceedance or survival function is then:

422
$$g\left(m\right) = \begin{cases} 1 - \dfrac{1 - e^{-\beta\left(m - M_w^m\right)}}{1 - e^{-\beta\left(M_w^M - M_w^m\right)}} & M_w^m \le m \le M_w^M \\ 0 & m > M_w^M \end{cases} \tag{16}$$

423   The M_w for the 1 million events are then obtained by sampling the truncated distribution within our region of interest,

424   *i.e.* M_w 7.5 to M_w 8.8 (see Figure 11a). The 1 million values of $\left(X_o, Y_o\right)$ are sampled from a uniform distribution

425   defined over the rectangle $[0\ L^{max}] \times [0\ W^{max}]$ of area $420\,km \times 129\,km$. Assuming a reduction of maximum mag-

426   nitude M_w^M from 8.8 to 8.6 gives a perturbed G-R relation (Figure 11a). In this case, the 1 million samples come from

427   the range M_w 7.5 to M_w 8.6. The histograms of 1 million samples for M_w are shown in Figure 11b. It also shows

428   10, 000 samples from the range M_w 7.5 to M_w 8.8 for performing comparisons.

429   To be able to generate 1 million predictions, we employ the efficiently implemented Multiple-Output Gaussian Process

430   emulator (MOGP)[6] from the Alan Turing Institute. Once the predictions are finished, we are left with two histograms

431   (one each for $\bar{v}_{max}$ and $\bar{\eta}_{max}$) at every virtual gauge, each made up of 1 million samples of predicted quantity. The

432   histograms are processed to extract $P_e\left(I\left(\boldsymbol{x}\right) \ge I_0\right)$, the probability of exceedance. P_e is the probability of the tsunami

433   having $I\left(\boldsymbol{x}\right) \ge I_0$ at a gauge $\boldsymbol{x}$. The intensity I is the measure of hazard, *i.e.* either $\bar{v}_{max}$ or $\bar{\eta}_{max}$, and I_0 is the intensity

434   threshold for the hazard quantity under consideration.

3. Results and Discussion

436   We first plot the raw output from the 1 million predictions, *i.e.* the histograms at 193 gauges in Figures 12a-b. At

437   each gauge, two histograms are superimposed on each other. These correspond to the two G-R relations with varying

438   maximum moment magnitude assumptions, *i.e.* M_w^M 8.6 and M_w^M 8.8 (Figure 11). The histograms also act as visual

439   indicators for the measure of the hazard at the gauge, and will be cast as hazard maps in Figure 14. Near the tip of

440   breakwaters and the mouth of the harbor, we observe relatively higher velocities than in other regions. We also observe

441   a complementary relation between the histograms of velocities and wave heights: the gauges having thicker histograms

442   for velocity have thinner histograms for wave heights and *vice versa*. These phenomena can also be observed in the

443   snapshots in Figure 8 (compare panels (b) & (c) with (h) & (i) respectively).

444   As expected, there is a clear reduction of hazard when the maximum moment magnitude is reduced. For closer

445   inspection, we enlarge the normalized histograms at gauge no. 91 in Figures 12c-d. Gauge no. 91 is located in the

---

[6]v0.2.0 available at *github.com/alan-turing-institute/mogp_emulator*

446 center of the map near the mouth of the port and is chosen since there is substantial spread of both maximum velocities

447 and wave heights in its histograms. In Figure 12c, the normalized histograms for maximum velocity are plotted.

448 The range of velocities for M_w 8.8 extends till $\sim 16\, ms^{-1}$, while it extends to only $\sim 6.2\, ms^{-1}$ for M_w 8.6. Thus, we

449 observe a $\sim 61\,\%$ reduction in maximum velocity hazard for a M_w 0.2 reduction in maximum moment magnitude. In

450 comparison, for the same reduction in maximum moment magnitude, the reduction in hazard from maximum wave

451 height is only $\sim 38\,\%$ (from $\sim 4.5\, m$ to $\sim 2.8\, m$ in Figure 12d). The probability of exceedance P_e that is extracted from

458 the histograms is plotted in the inset of the respective figure.

459   Figures 13a-b compare normalized histograms for 1 million and 10,000 samples of input parameters (see Figure

460 11b). The corresponding probability of exceedance P_e plots with their 99% confidence intervals can be seen in the

461 inset. In Figure 13a, we observe that the histogram corresponding to 10,000 predictions is curtailed around $7.5\, ms^{-1}$

462 and becomes very sparse for higher velocities. This is due to a deficit of samples that results in the isolated bars for

463 higher velocities. This behaviour also translates into larger uncertainties (or wider confidence intervals) for estimates

464 of low probabilities of P_e. In contrast, 1 million predictions adequately sweep through the entire range of velocities

465 resulting in lower uncertainties (or narrower confidence intervals) for the tail probabilities. It may be noted that tail

466 probabilities in the P_e curve correspond to extreme events with higher velocities. Similar behaviour is seen in Figure

467 13b, where the deficit of samples is observed for maximum wave heights higher than $2.7\, ms^{-1}$ for the case of 10,000

468 predictions.

469 In Figures 13c-d, we plot the probability of exceedance curves extracted from the histograms of 1 million predictions

470 for the 193 gauges. Superimposed on top are the P_e curves for 10,000 predictions. The horizontal lines in the plots

471 are the chosen values of probability of exceedance, 10^{-1}, 10^{-2} and 10^{-3}, progressively decreasing by an order of

472 magnitude. The vertical lines in Figure 13c denote maximum velocities of 1.5, 3.1 and $4.6\, ms^{-1}$ (or 3, 6 and 9 knots

473 respectively), values that demarcate categories of damage in Figure 1 of Lynett et al. (2014). The vertical lines in

474 Figure 13c denote maximum wave heights of 0.75, 1.5 and $3\, m$. These values are used to construct hazard maps in

475 Figure 14. In both Figures 13c-d, the reach of the P_e curve is extended beyond the low probability of 10^{-4} to include

476 even extreme events only in the case of 1 million predictions. Additionally, although the lower probabilities (around

477 10^{-4}) have been made accessible by 10 thousand events, they require 1 million events for accurate resolution: with

478 only 10,000 samples, both probabilities and quantities are overestimated between 10^{-3} and 10^{-4}. Hence, being able to

479 produce a very large number of predictions is crucial to hazard assessment. Only with the utilization of the emulator

480 – needing only 300 simulations – are we able to afford realistic predictions of velocities and wave heights at high

481 resolution.

482 Port hazard maps were developed for Crescent City, California (Lynett et al., 2014) and four sites in New Zealand

483 (Borrero et al., 2015a). The hazard was represented on the maps by velocity zonations, a time-threshold metric and
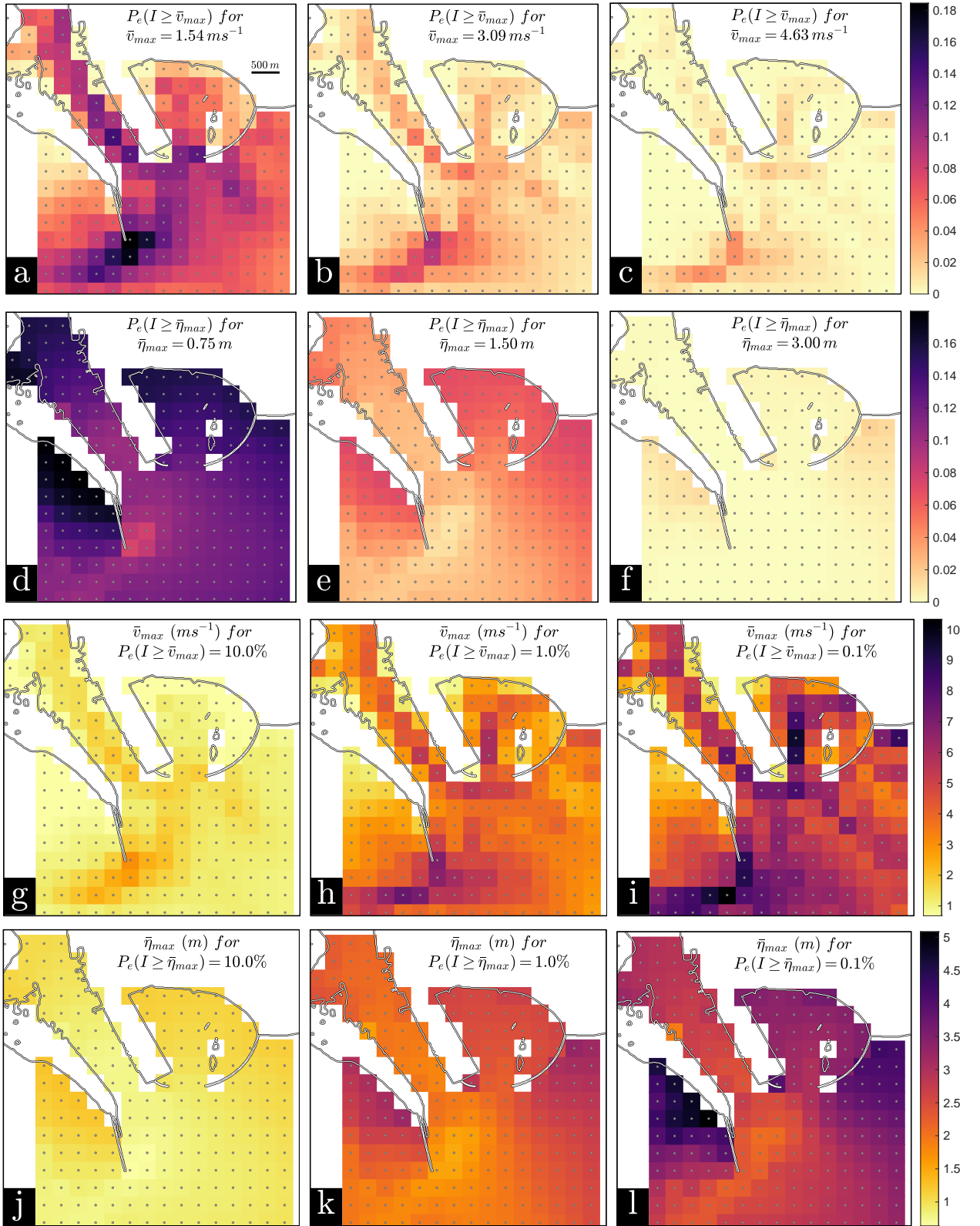
Figure 14: Hazard maps. a-c) Probability of exceedance at the 193 gauges for three chosen values of predicted maximum velocities $\bar{v}_{max}$. d-f) Predicted maximum velocities for three given probabilities of exceedance. g-l) Same as (a)-(f) but for predicted maximum wave heights $\bar{\eta}_{max}$.

484 safe depths for vessel evacuation. Here, the probability of exceedance curves in Figure 13 are cast as hazard maps

485 in Figure 14, more along the lines of Gonzalez et al. (2013) and Park and Cox (2016). We plot the probability of

486 exceedance at the 193 gauges on the map for the chosen values of maximum velocities in Figures 14a-c. Similar plots

487 for chosen values of maximum wave heights are shown in Figures 14d-f. For both velocities and wave heights, the

488 overall probability decreases as the intensity threshold increases. Specifically, the bulk of P_e for maximum velocities

489 is concentrated at the tip of breakwaters and along the dredged channel leading into the port (seen in port bathymetry,

490 Figure 6j), as also observed in (Lynett et al., 2012). This is also supported by the patterns of localised higher maximum

491 velocities in Figures 8a & d. In contrast, the spatial distribution of P_e for maximum wave height shows a complementary

492 behaviour and is more spread out.

493   Conversely, for chosen probabilities of exceedance, the corresponding hazard thresholds at the gauges are plotted

494 in Figures 14g-l. As expected, the overall intensity thresholds increase with decrease in probability of exceedance.

495 Again, the bulk of the maximum velocity threshold is concentrated at the tip of breakwaters and along the dredged

496 channel (Figures 14g-i). Here too, we see a complementary behaviour for maximum wave height in Figures 14j-l.

497   Arcos and LeVeque (2015) found that velocities have more spatial variation than heights. Dengler and Uslu (2011)

498 showed increased sensitivity of velocities to port configurations, compared to wave heights. The larger spatial variation

499 of velocities in Figure 13c compared to wave heights in Figure 13d is evident in the probability of exceedance plotted

500 for all the gauges. This can be attested in Figures 12a-b, where the bulkiness of velocity histograms varies spatially

501 much more than that of the heights. Additionally, at a given gauge, we observe that the spread of velocities is much

502 more than those of the heights for the same set of earthquake scenarios, *e.g.* compare Figures 12a-b for gauge no. 91.

503 These behaviours can also be deduced for individual runs from the spatial variations of maximum velocity and wave

504 height is Figure 8 (compare panels (a) & (d) with (g) & (j) respectively).

505 The probability of exceedance extracted in this work acts as the basic input for common hazard outputs of probability of

506 occurrence (and return periods), especially the ~ 2475 year mean return period for the Maximum Considered Tsunami

507 (MCT) as laid out in Chapter 6 of ASCE 7-16 (Chock, 2016). It also feeds into loss estimation functions (Muhari

508 et al., 2015). But a full probabilistic assessment would ideally need to include further sources of uncertainties. These

509 include layers of uncertainties that are either epistemic or aleatoric in nature. Epistemic uncertainties include the scal-

510 ing relation, and the Gutenberg-Richter approximation of the occurrence-magnitude relationship (Davies et al., 2018),

511 *i.e.* both the maximum moment magnitude and the *b*-value. The major influence of the maximum magnitude was

512 illustrated in initial work by Hoechner et al. (2016), but for a simplified tsunami modeling strategy. Here, we only

513 assess two cases, for M_w^M 8.6 and M_w^M 8.8. Uncertainties in the bathymetry near shore have also been shown to have

514 a large influence on tsunamis at the shore (Liu and Guillas, 2017). Combining the tools of dimension reduction and

515 emulation, such a modeling of the epistemic uncertainty would be beneficial to include.

516 Aleatoric uncertainties in the variations of the geometry in the seafloor uplift and subsidence can be readily incor-

517 porated. An alternative to our slip profile generation is to directly parameterize the co-seismic deformation profile

518 using 3 parameters as in Guillas et al. (2018) (or more) to vary the geometry more freely and be more realistic. The

519 Okada model that transforms the slips to the vertical deformation is then bypassed. This route is quite attractive since

520 it allows the creation of very realistic deformation patterns with a fixed number of parameters, and does away with the

521 dependency of the deformation/slip on the resolution of the segmentation (shown in Figure 3b inset).

522 Our work uniformly samples the 1 million samples for rupture origin co-ordinates (another aleatoric uncertainty).

523 However, a recent spatial distribution of locking has been made available for the MSZ (Frohling and Szeliga, 2016).

524 It would be even more realistic to sample the rupture origin coordinates using the locking distribution, since zones of

525 high locking act as a major cause for earthquake reoccurence as recently hypothesised in Moernaut et al. (2018). The

526 locations could be further distributed based on the depth dependent rigidity (Scala et al., 2019).

527 Randomness in tide levels at the time of impact (consequent changes of up to 25% reported in Ayca and Lynett (2016))

528 could be included, as well as the numerical error in the approximation of the currents since our depth-averaged model

529 is 2-D but 3-D modeling will increase precision, and account for vertical vorticity (Lynett et al., 2017; Lynett, 2016).

530 Better designs of computer experiments than the Latin Hypercube Design used here could be employed to reduce

531 uncertainties in the emulator's approximation, such as sequential design (Beck and Guillas, 2016) already used for

532 tsunamis with success and is now implemented in an advanced computational workflow.

533 Instead of investigating a range of scenarios, if one only wants to examine the maximum wave height in order to build

534 defences for instance, a recent surrogate-based optimization could be pursued whereby the design of experiment is

535 combined with a search for the maximum, saving large quantities of computational time and increasing accuracy due

536 to the focus on the optimization (Mathikolonis et al., 2019). To be able to emulate a sequence of multiple models of

537 seabed deformation and tsunami propagation, and possibly a 3-D model of currents locally, a new approach, called

538 integrated emulation (Ming and Guillas, 2019) allows even better designs where the most influential models are run

539 more times where it matters, and where the integrated emulator propagates uncertainties with higher fidelity by tak-

540 ing into account the intermediate models in the system of simulators. This approach has the potential to enable fully

541 realistic end-to-end coupling of 3-D earthquake sources models with tsunami models (Ulrich et al., 2019).

4. Conclusions

543   In this paper, we provide a novel end-to-end quantification of uncertainties of future earthquake-generated tsunamis

544 heights and currents in the MSZ:

545   1. We replace the complex, expensive high-resolution tsunami simulator by a functionally simple, cheap statistical

546   emulator trained using 300 tsunami simulations at 10 m mesh resolution in the vicinity of the port. We propagate

547   uncertainties from the Gutenberg-Richter relation to tsunami impacts of maximum velocities and wave heights

548   in the port area of Karachi, Pakistan. We observe maximum (extreme event) velocities and wave heights of up

549   to $16\,ms^{-1}$ and $8\,m$ respectively for the range $M_w\,7.5 - 8.8$ (Figure 12).

2. We perform the largest emulation using 1 million predictions/source scenarios. To our knowledge, this is the first large-scale uncertainty quantification of earthquake-generated tsunami current hazard. We are able to display the necessity of this very large number of predictions for resolving very low probabilities of exceedance ($< 10^{-3}$) - very high impact extreme events ($v_{max} > 7.5\,ms^{-1}$ and $\eta_{max} > 3\,m$) with tighter uncertainties (Figure 13).

3. We observe that reduction in hazard due to a reduction in maximum moment magnitude is more for velocities than wave heights. Near the mouth of the harbor, the reduction in hazard is $\sim 61\,\%$ for maximum velocity, but only $\sim 38\,\%$ for maximum wave height (corresponding to a reduction in maximum moment magnitude from 8.8 to 8.6) (Figure 13c).

4. We generate the first area-wide probabilistic hazard maps of tsunami currents from 1 million predicted scenarios at the Karachi port (Figures 14a-f). It shows patterns that are geophysically meaningful and important for the next steps of disaster risk reduction. We identify concentrations of high probability of exceedance around the port for given intensity threshold (a maximum of $\sim 18\,\%$, $10\,\%$ and $4\,\%$ for 3, 6 and 9 knots respectively) (Figures 14a-c). Conversely, the same regions also have high intensity thresholds given probability of exceedance (a maximum of ~ 3.1, 7.5 and $10.3\,ms^{-1}$ for $10\,\%$, $1\,\%$ and $0.1\,\%$ respectively) (Figures 14d-f). Overall, without our large-scale emulation, such outputs would be impractical to produce due to computational costs.

5. We display more spatial variations for maximum velocity compared to wave heights around the port and their complementary behaviour for the aggregate of 1 million scenarios (Figures 8, 12, 13 and 14).

A. Slip Profile Generation

568   Select the dimension (h_s) of a FF segment based on: (i) computational effort required – increases as h_s decreases,

569 along $O\left(n_F^2\right) \sim O\left(h_s^{-2}\right)$, (ii) fidelity to the scaling relation (Figure 3b inset) – earthquake dimensions are resolved to

570 $O\left(h_s\right)$ (Figure 3b). We select $h_s \sim 5\,km$, which for the overall FF dimensions of $L^{max} \sim 420\,km$ and $W^{max} \sim 129\,km$

571 results in 2295 segments. With the segment dimension h_s, use the scaling relation to determine the minimum M_w

572 that can be accommodated on the FF. To resolve the slip profile adequately, we require a fault to span a minimum

573 of 4 segments in both the length and width directions. This results in a minimum M_w of 6.32. This is sufficient as

574 our region of investigation starts at $M_w^{min} = 7.5$. For the FF model of area $L^{max} \times W^{max}$, use the scaling relation to

575 determine the maximum M_w that can be accommodated on the FF. We get the maximum M_w as $M_w^{sat} = 8.65$ (Figure

576 3a). Since our region of investigation is till M_w 8.8, for ruptures with $M_w > M_w^{sat}$, we saturate the slip on the fault

577 with M_w^{sat}. Algorithm 1 and Figures 4b-d detail the slip profile generation given the input parameter $\left(M_w, X_o, Y_o\right)$.

Algorithm 1 Slip profile generation

1: For a given earthquake moment magnitude M_w, and rupture origin co-ordinates (X_o, Y_o) (Figure 3a inset); find the rupture length L and width W from the scaling relation. The co-ordinates have their origin as the south-west corner of the FF (Figure 3a inset).

2: Fit the fault rectangle of size $L \times W$ into the FF. There are two possibilities with the rupture origin (X_o, Y_o) being located at :
(i) the centre of the fault and equidistant from the boundaries of the fault rectangle, *i.e.* with distances $L/2$ and $W/2$.
(ii) not the centre of the fault. In this case, (X_o, Y_o) is at different distances from the boundaries of the fault rectangle.

3: Use Eqn. 3 to construct the lobes $\phi(x; r_E, \alpha)$ and $\phi(x; r_W, \alpha)$ and form the bi-lobed kernel function for fault length $\Phi(x; r_W, r_E, \alpha)$ (Figure 4b). Similarly, form the bi-lobed kernel function for fault width $\Phi(x; r_N, r_S, \alpha)$ by constructing the lobes $\phi(x; r_N, \alpha)$ and $\phi(x; r_S, \alpha)$ (Figure 4d). r_E, r_W, r_N and r_S are the distances of earthquake origin from the eastern, western, northern and southern sides of the fault rectangle.

4: Use Eqn. 4 to construct the tensor product $\Phi^{\otimes}$ of the two bi-lobed kernel functions in the previous step. $\Phi^{\otimes}$ will entirely reside within the fault rectangle and will become 0 at its boundaries (Figure 4c).

5: Multiply the values of $\Phi^{\otimes}$ at the centres of each segment (*i.e.* $\Phi_i^{\otimes}$) with a factor $M_w \left(\sum_{i=1}^{n_F} \mu l_i w_i \Phi_i^{\otimes} \right)^{-1}$ to get the slip S_i on the segment. This normalization results in the slips in the fault rectangle to have a combined moment magnitude of M_w.

B. Merging Bathymetry Data from Hydrographic Chart, SRTM, GEBCO and Satellite Imagery

The four data sets that are used to create the merged bathymetry for computational mesh generation (Section 2.4.2) and tsunami simulations (Section 2.4) are at different resolutions – $\sim 1'' \sim 30\,m$ (digitized hydrographic charts and SRTM v3), $\sim 15'' \sim 450\,m$ (GEBCO 2019), and $\sim 10\,m$ (coastline features in satellite imagery from Google Earth). The digitized chart data is available in the domain of interest (DOI) $[66.9332, 67.0168]° E \times [24.7666, 24.8334]° N$. The cosine-tapered Tukey window used in the merging process is given by:

$$\theta(x, r_c) = \begin{cases} \frac{1}{2}\left\{ 1 + \cos\left(\frac{2\pi}{r_c}\left[x - r_c/2 \right] \right) \right\} & 0 \leq x \leq \frac{r_c}{2} \\ 1 & \frac{r_c}{2} \leq x \leq 1 - \frac{r_c}{2} \\ \frac{1}{2}\left\{ 1 + \cos\left(\frac{2\pi}{r_c}\left[x - 1 + r_c/2 \right] \right) \right\} & 1 - \frac{r_c}{2} \leq x \leq 1 \end{cases} \tag{B.1}$$

where r_c is the ratio of length of cosine-taper to the total window length of 1. Shifted and dilated versions of θ are used to create the tensor product:

$$\Theta\left(x - x_p, y - y_p, d_x, d_y, r_c^x, r_c^y \right) = \theta\left(\frac{x - x_p}{d_x}, r_c^x \right) \otimes \theta\left(\frac{y - y_p}{d_y}, r_c^y \right) \tag{B.2}$$

608 where (x_p, y_p) and $d_x \times d_y$ are co-ordinates of the centre and area of the DOI respectively, whilst (r_c^x, r_c^y) are the cosine-

609 fractions along the length and width of the DOI. Algorithm 2 and Figure 6 detail the procedure used for merging the

610 different bathymetries.

Algorithm 2 Merging bathymetry data

611

612 1: Up-sample the hydrographic chart data and GEBCO bathymetry in the DOI on a rectangular grid having a reso-
613   lution of the computational mesh ($\sim 10\,m$) (Figures 6a & d respectively).

614 2: Integrate the polygonal domains of resolved coastline features into up-sampled bathymetry by filling land areas
615   with a positive constant ($2\,m$) (Figure 6b).

616 3: Interpolate the SRTM data for land onto the grid. If SRTM data exists on the water area after integration of port
617   features, discard the SRTM data there (Figure 6c).

618 4: Construct tensor product of cosine-tapered Tukey windows (Θ) and its complement ($1 - \Theta$) with cosine fractions
619     $r_c^x = r_c^y = 10\,\%$ (Figures 6f & 6g respectively).

620 5: Multiply hydrographic chart data integrated with port coastline features and SRTM data (Figure 6c) with Θ (Figure
621   6f) to get windowed merged bathymetry (Figure 6h). The data at the start of the taper is used for the tapered region.

622

623 6: Multiply GEBCO 2019 data (Figure 6d) with $1 - \Theta$ (Figure 6g) to get windowed GEBCO bathymetry (Figure 6i).

624

625 7: Add windowed merged bathymetry (Figure 6h) with windowed GEBCO bathymetry (Figure 6i) to get the final
626   merged bathymetry (Figure 6j).

C. Localised Non-Uniform Unstructured Mesh

627

628   The mesh sizing function h that is fed into Gmsh is constructed in three stages, *viz.* offshore, onshore and port

629 regions. For offshore mesh, the design criteria is based on the bathymetry b (Figure 7a inset). Some more steps are

630 required after the definition of h_λ in Eqn. 14 of Section 2.4.2. The mesh sizing h_λ defined in Eqn. 14 may turn out to

631 be too steep (green curve in Figure 7a), or having a a high gradient with respect to the bathymetry b. A reduction is

632 gradient is achieved by interpolating between the triangle size λ_o/n_h at b_o and the minimum mesh size h_m at the coast,

633 *i.e.* $b = 0$ (red curve in Figure 7a):

634
$$h_I(b) = b(\boldsymbol{x}) * \left(\lambda_o/n_h - h_m\right) / \left(b_o - 0\right) + h_m \tag{C.1}$$

635 The mesh sizing function $h(b)$ is then given by the minimum:

636
$$h(b) = \min\left(h_\lambda(b), h_I(b)\right) \tag{C.2}$$

637   Next, the design criteria for the onshore mesh sizing function $h(\pi)$ is based on the coast proximity $\pi(\boldsymbol{x})$ defined

638 as the minimum distance of a point $\boldsymbol{x}$ from the coastline C of the merged bathymetry (Figure 7b inset):

639
$$\pi(\boldsymbol{x}) = \min_{\boldsymbol{x}_c \in C} \left\| \boldsymbol{x} - \boldsymbol{x}_c \right\|_2 \tag{C.3}$$

---

640   The mesh sizing function is broken into three regions, *viz.* inundation, stretch and blow-up regions (Figure 7b). In

641   the inundation region which extends inland for a distance π_I (2.5 *km*) from the coast, the mesh size is prescribed as

642   the minimum mesh size h_m (500 *m*). Thus, the inundation region acts as a smooth transitioning region between the

643   onshore and offshore mesh. Further inland away from the inundation region, we require the triangle sizes to explode

644   quickly to the maximum mesh size h_M (25 *km*). This region is called the blow-up region (from π_S to π_B in Figure

645   7b). Since such a transition needs to happen in a smooth manner, we introduce the stretch region between the end of

646   the inundation region and the beginning of the blow-up region (from π_I to π_S in Figure 7b). In the stretch region the

647   triangle size transitions from h_m to h_S (10 *km*). To prescribe mesh sizes in the stretch region, we define the *size ratio*

648   ρ (= 1.3) to be the ratio of sizes of adjacent triangle in the mesh (also called *grading gauge* in Legrand et al. (2006)).

649   The stretch distance $\pi_S - \pi_I$ is calculated as:

$$\pi_S - \pi_I = h_m + \rho h_m + \rho^2 h_m + \ldots + \rho^{n_S} h_m \tag{C.4}$$

651   Eqn. C.4 is a geometric series that approximates the distance by summing up the sizes of $n_S + 1$ triangles, lined up

652   end-to-end in a straight line, progressively increasing in size by a factor of ρ (Legrand et al., 2006), starting from h_m

653   to $\rho^{n_S} h_m$. Equating the last term to h_S, solves for integer n_S as:

$$n_S = \lceil \log_\rho \left(\frac{h_S}{h_m} \right) \rceil \tag{C.5}$$

655   where $\lceil \cdot \rceil$ denotes the ceiling function. Similarly, the blow-up distance $\pi_B - \pi_S$ is calculated as:

$$\pi_B - \pi_S = h_S + \rho h_S + \rho^2 h_S + \ldots + \rho^{n_B} h_S \tag{C.6}$$

657   Similar to Eqn. C.4, Eqn. C.6 is a geometric series summing up the sizes of $n_B + 1$ triangles, progressively increasing

658   in size from h_S to $\rho^{n_B} h_S$, by a factor of ρ. Equating the last term to h_M, solves for integer n_B as:

$$n_B = \lceil \log_\rho \left(\frac{h_M}{h_S} \right) \rceil \tag{C.7}$$

660   The mesh sizing function is specified to Gmsh on a background rectangular mesh. The resolution of the background

661   mesh is half the resolution of GEBCO grid, *i.e.* ~210 *m*, sufficient for specifying the h_m of 500 *m*. Each of the above

662   mesh sizings for the inundation, stretch and blow-up regions need to be specified on the background mesh. The number

663   of levels mentioned in Figure 7b are the number of grids in the background mesh needed to specify mesh sizes in the

664   respective region.

665   Finally, the mesh sizing function is constructed in the vicinity of the port (Figure 7h-j). The strategy followed is

666 similar to offshore mesh sizing, but instead of the proximity to coast, the radial distance from the centre (x_p, y_p) of

667 the DOI (or port) is used. A ρ^p of 1.05 is chosen for a very smooth transition of mesh. The mesh sizing is fixed at

668 h_m^p (10 m) for the DOI where the resolved bathymetry is available. The resolution of background mesh near the port is

669 kept at 10 m, *i.e.* at least same as h_m^p. In increasing radii extending outwards from the DOI, the mesh sizing increases

670 similar to Eqn. C.4 but iteratively with increasing number of terms. The iterative procedure is employed to ensure

671 that there is a smooth merging of the mesh sizing function at the port with existing offshore and onshore mesh sizing

672 functions.

CRediT authorship contribution statement

Acknowledgments

695 for smooth installation and running of VOLNA-OP2 on CSD3. We also acknowledge fruitful discussions with Deyu

696 Ming and Mariya Mamajiwala on truncated G-R distribution and prediction intervals for L-O-O diagnostics, Frédéric

697 Dias on meshing strategies and sediment amplification curve, Theodoros Mathikolonis on emulation, and Simon Day,

698 Kusala Rajendran and C.P. Rajendran on seismicity of MSZ. We thank David H. Hickcox for permission to reproduce

699 his photograph of *Maersk Mandraki* in Figure 1d.

References

701 Allen, T.I., Hayes, G.P., 2017. Alternative rupture-scaling relationships for subduction interface and other offshore environments. Bulletin of the

702   Seismological Society of America 107, 1240–1253. doi:10.1785/0120160255.

703 Arcos, M.E.M., LeVeque, R.J., 2015. Validating velocities in the GeoClaw tsunami model using observations near Hawaii from the 2011 Tohoku

704   tsunami. Pure and Applied Geophysics 172, 849–867. doi:10.1007/s00024-014-0980-y.

705 Ayca, A., Lynett, P.J., 2016. Effect of tides and source location on nearshore tsunami-induced currents. Journal of Geophysical Research: Oceans

706   121, 8807–8820. doi:10.1002/2016JC012435.

707 Battaglia, M., Cervelli, P., Murra-Muraleda, J., 2012. Modeling crustal deformation_A catalog of deformation models and modeling approaches.

708   US Geological Survey Techniques and Methods , 37–85.

709 Battaglia, M., Cervelli, P.F., Murray, J.R., 2013. dMODELS: A MATLAB software package for modeling crustal deformation near active faults

710   and volcanic centers. Journal of Volcanology and Geothermal Research 254, 1 – 4.

711 Beck, J., Guillas, S., 2016. Sequential design with Mutual Information for Computer Experiments (MICE): Emulation of a tsunami model.

712   SIAM/ASA Journal on Uncertainty Quantification 4, 739–766. doi:10.1137/140989613.

713 Blaser, L., Krüger, F., Ohrnberger, M., Scherbaum, F., 2010. Scaling relations of earthquake source parameter estimates with special focus on

714   subduction environment. Bulletin of the Seismological Society of America 100, 2914–2926. doi:10.1785/0120100111.

715 Borrero, J.C., Goring, D.G., Greer, S.D., Power, W.L., 2015a. Far-field tsunami hazard in New Zealand ports. Pure and Applied Geophysics 172,

716   731–756. doi:10.1007/s00024-014-0987-4.

717 Borrero, J.C., Lynett, P.J., Kalligeris, N., 2015b. Tsunami currents in ports. Philosophical Transactions of the Royal Society A: Mathematical,

718   Physical and Engineering Sciences 373, 20140372. doi:10.1098/rsta.2014.0372.

719 Byrne, D.E., Sykes, L.R., Davis, D.M., 1992. Great thrust earthquakes and aseismic slip along the plate boundary of the Makran Subduction Zone.

720   Journal of Geophysical Research: Solid Earth 97, 449–478. doi:10.1029/91JB02165.

721 Chock, G.Y.K., 2016. Design for tsunami loads and effects in the ASCE 7-16 standard. Journal of Structural Engineering 142, 04016093. doi:10.

722   1061/(ASCE)ST.1943-541X.0001565.

723 Cosentino, P., Ficarra, V., Luzio, D., 1977. Truncated exponential frequency-magnitude relationship in earthquake statistics. Bulletin of the

724   Seismological Society of America 67, 1615–1623.

725 Danciu, L., et al., 2018. The 2014 earthquake model of the Middle East: seismogenic sources. Bulletin of Earthquake Engineering 16, 3465–3496.

726   doi:10.1007/s10518-017-0096-8.

727 Davies, G., et al., 2018. A global probabilistic tsunami hazard assessment from earthquake sources. Geological Society, London, Special Publications

728   456, 219–244. doi:10.1144/SP456.5.

729 Dengler, L., Uslu, B., 2011. Effects of harbor modification on Crescent City, California's tsunami vulnerability. Pure and Applied Geophysics 168,

730   1175–1185. doi:10.1007/s00024-010-0224-8.

731 Dias, F., Dutykh, D., ÓBrien, L., Renzi, E., Stefanakis, T., 2014. On the modelling of tsunami generation and tsunami inundation. Procedia IUTAM

732 10, 338 – 355. doi:10.1016/j.piutam.2014.01.029. mechanics for the World: Proceedings of the 23rd International Congress of Theoretical

733 and Applied Mechanics, ICTAM2012.

734 Dutykh, D., Dias, F., 2010. Influence of sedimentary layering on tsunami generation. Computer Methods in Applied Mechanics and Engineering

735 199, 1268 – 1275. doi:10.1016/j.cma.2009.07.011. multiscale Models and Mathematical Aspects in Solid and Fluid Mechanics.

736 Dutykh, D., Poncet, R., Dias, F., 2011. The VOLNA code for the numerical modeling of tsunami waves: Generation, propagation and inundation.

737 European Journal of Mechanics - B/Fluids 30, 598 – 615. doi:10.1016/j.euromechflu.2011.05.005. special Issue: Nearshore Hydrody-

738 namics.

739 Frohling, E., Szeliga, W., 2016. GPS constraints on interplate locking within the Makran subduction zone. Geophysical Journal International 205,

740 67–76. doi:10.1093/gji/ggw001.

741 GEBCO Bathymetric Compilation Group 2019, 2019. The GEBCO_2019 Grid - a continuous terrain model of the global oceans and land. doi:10/

742 c33m.

743 Geuzaine, C., Remacle, J.F., 2009. Gmsh: A 3-D finite element mesh generator with built-in pre- and post-processing facilities. International

744 Journal for Numerical Methods in Engineering 79, 1309–1331. doi:10.1002/nme.2579.

745 Giles, D., Kashdan, E., Salmanidou, D.M., Guillas, S., Dias, F., 2020. Performance analysis of Volna-OP2 – massively parallel code for tsunami

746 modelling. arXiv preprint arXiv:2002.04889 .

747 Gonzalez, F.I., LeVeque, R.J., Adams, L.M., 2013. Probabilistic Tsunami Hazard Assessment (PTHA) for Crescent City, CA. Final Report for

748 Phase I. Technical Report. University of Washington Department of Applied Mathmatics.

749 Grezio, A., Babeyko, A., Baptista, M.A., Behrens, J., Costa, A., Davies, G., Geist, E.L., Glimsdal, S., González, F.I., Griffin, J., Harbitz, C.B.,

750 LeVeque, R.J., Lorito, S., Løvholt, F., Omira, R., Mueller, C., Paris, R., Parsons, T., Polet, J., Power, W., Selva, J., Sørensen, M.B., Thio, H.K.,

751 2017. Probabilistic tsunami hazard analysis: Multiple sources and global applications. Reviews of Geophysics 55, 1158–1198. doi:10.1002/

752 2017RG000579.

753 Guillas, S., Sarri, A., Day, S.J., Liu, X., Dias, F., et al., 2018. Functional emulation of high resolution tsunami modelling over Cascadia. The Annals

754 of Applied Statistics 12, 2023–2053. doi:10.1214/18-AOAS1142.

755 Hanks, T.C., Kanamori, H., 1979. A moment magnitude scale. Journal of Geophysical Research: Solid Earth 84, 2348–2350. doi:10.1029/

756 JB084iB05p02348.

757 Hasan, H., Lodhi, H., LeVeque, R., Lodhi, S., Ahmed, S., 2017. Assessing tsunami risk to Karachi Port through simulation of currents that were

758 reportedly produced there by the 1945 Makran tsunami, in: Proceedings of the 16th world conference on earthquake engineering, Santiago,

759 Chile.

760 Hayes, G.P., 2018. Slab2 - A Comprehensive Subduction Zone Geometry Model: U.S. Geological Survey data release. doi:10.5066/F7PV6JNV.

761 Hayes, G.P., Moore, G.L., Portner, D.E., Hearne, M., Flamme, H., Furtney, M., Smoczyk, G.M., 2018. Slab2, a comprehensive subduction zone

762 geometry model. Science 362, 58–61. doi:10.1126/science.aat4723.

763 Heidarzadeh, M., Kijko, A., 2011. A probabilistic tsunami hazard assessment for the Makran subduction zone at the northwestern Indian Ocean.

764 Natural Hazards 56, 577–593. doi:10.1007/s11069-010-9574-x.

765 Heidarzadeh, M., Pirooz, M.D., Zaker, N.H., Yalciner, A.C., Mokhtari, M., Esmaeily, A., 2008. Historical tsunami in the Makran Subduction Zone

766 off the southern coasts of Iran and Pakistan and results of numerical modeling. Ocean Engineering 35, 774 – 786. doi:10.1016/j.oceaneng.

767 2008.01.017.

768 Heidarzadeh, M., Satake, K., 2014. Possible sources of the tsunami observed in the northwestern Indian Ocean following the 2013 September 24

769   Mw 7.7 Pakistan inland earthquake. Geophysical Journal International 199, 752–766. doi:10.1093/gji/ggu297.

770   Hoechner, A., Babeyko, A.Y., Zamora, N., 2016. Probabilistic tsunami hazard assessment for the Makran region with focus on maximum magnitude
771   assumption. Natural Hazards and Earth System Sciences 16, 1339–1350. doi:10.5194/nhess-16-1339-2016.

772   Kanamori, H., 1977. The energy release in great earthquakes. Journal of Geophysical Research (1896-1977) 82, 2981–2987. doi:10.1029/
773   JB082i020p02981.

774   Legrand, S., Deleersnijder, E., Hanert, E., Legat, V., Wolanski, E., 2006. High-resolution, unstructured meshes for hydrodynamic models of the
775   Great Barrier Reef, Australia. Estuarine, Coastal and Shelf Science 68, 36 – 46. doi:10.1016/j.ecss.2005.08.017.

776   Liu, X., Guillas, S., 2017. Dimension reduction for Gaussian process emulation: An application to the influence of bathymetry on tsunami heights.
777   SIAM/ASA Journal on Uncertainty Quantification 5, 787–812. doi:10.1137/16M1090648.

778   Lynett, P.J., 2016. Precise prediction of coastal and overland flow dynamics: A grand challenge or a fool's errand. Journal of Disaster Research 11,
779   615–623. doi:10.20965/jdr.2016.p0615.

780   Lynett, P.J., Borrero, J., Son, S., Wilson, R., Miller, K., 2014. Assessment of the tsunami-induced current hazard. Geophysical Research Letters
781   41, 2048–2055. doi:10.1002/2013GL058680.

782   Lynett, P.J., Borrero, J.C., Weiss, R., Son, S., Greer, D., Renteria, W., 2012. Observations and modeling of tsunami-induced currents in ports and
783   harbors. Earth and Planetary Science Letters 327-328, 68 – 74. doi:10.1016/j.epsl.2012.02.002.

784   Lynett, P.J., et al., 2017. Inter-model analysis of tsunami-induced coastal currents. Ocean Modelling 114, 14 – 32. doi:10.1016/j.ocemod.2017.
785   04.003.

786   Mathikolonis, T., Roeber, V., Guillas, S., 2019. Computationally efficient surrogate-based optimization of coastal storm waves heights and run-ups.
787   arXiv preprint arXiv:1910.01932 .

788   Ming, D., Guillas, S., 2019. Integrated emulators for systems of computer models. arXiv preprint arXiv:1912.09468 .

789   Moernaut, J., Daele, M.V., Fontijn, K., Heirman, K., Kempf, P., Pino, M., Valdebenito, G., Urrutia, R., Strasser, M., Batist, M.D., 2018. Larger
790   earthquakes recur more periodically: New insights in the megathrust earthquake cycle from lacustrine turbidite records in south-central Chile.
791   Earth and Planetary Science Letters 481, 9 – 19. doi:10.1016/j.epsl.2017.10.016.

792   Muhari, A., Charvet, I., Tsuyoshi, F., Suppasri, A., Imamura, F., 2015. Assessment of tsunami hazards in ports and their impact on marine vessels
793   derived from tsunami models and the observed damage data. Natural Hazards 78, 1309–1328. doi:10.1007/s11069-015-1772-0.

794   Okada, Y., 1985. Surface deformation due to shear and tensile faults in a half-space. Bulletin of the Seismological Society of America 75, 1135–1154.

795   Okal, E.A., Fritz, H.M., Raad, P.E., Synolakis, C., Al-Shijbi, Y., Al-Saifi, M., 2006. Oman field survey after the December 2004 Indian Ocean
796   tsunami. Earthquake Spectra 22, 203–218. doi:10.1193/1.2202647.

797   Park, H., Cox, D.T., 2016. Probabilistic assessment of near-field tsunami hazards: Inundation depth, velocity, momentum flux, arrival time, and
798   duration applied to Seaside, Oregon. Coastal Engineering 117, 79 – 96. doi:10.1016/j.coastaleng.2016.07.011.

799   Rashidi, A., Shomali, Z.H., Dutykh, D., Keshavarz Farajkhah, N., 2020. Tsunami hazard assessment in the Makran subduction zone. Natural
800   Hazards 100, 861–875. doi:10.1007/s11069-019-03848-1.

801   Reguly, I.Z., et al., 2018. The VOLNA-OP2 tsunami code (version 1.5). Geoscientific Model Development 11, 4621–4635. doi:10.5194/
802   gmd-11-4621-2018.

803   Salmanidou, D.M., Guillas, S., Georgiopoulou, A., Dias, F., 2017. Statistical emulation of landslide-induced tsunamis at the Rockall Bank, NE
804   Atlantic. Proceedings of the Royal Society A: Mathematical, Physical and Engineering Sciences 473, 20170026. doi:10.1098/rspa.2017.
805   0026.

806   Salmanidou, D.M., Heidarzadeh, M., Guillas, S., 2019. Probabilistic landslide-generated tsunamis in the Indus Canyon, NW Indian Ocean, using

807   statistical emulation. Pure and Applied Geophysics 176, 3099–3114. doi:10.1007/s00024-019-02187-3.

808   Scala, A., Lorito, S., Romano, F., Murphy, S., Selva, J., Basili, R., Babeyko, A., Herrero, A., Hoechner, A., Løvholt, F., Maesano, F.E., Perfetti,
809   P., Tiberti, M.M., Tonini, R., Volpe, M., Davies, G., Festa, G., Power, W., Piatanesi, A., Cirella, A., 2019. Effect of shallow slip amplification
810   uncertainty on probabilistic tsunami hazard analysis in subduction zones: Use of long-term balanced stochastic slip models. Pure and Applied
811   Geophysics doi:10.1007/s00024-019-02260-x.

812   van Scheltinga, A.D.T., Myers, P.G., Pietrzak, J.D., 2012. Mesh generation in archipelagos. Ocean Dynamics 62, 1217–1228. doi:10.1007/
813   s10236-012-0559-z.

814   Smith, G.L., McNeill, L.C., Wang, K., He, J., Henstock, T.J., 2013. Thermal structure and megathrust seismogenic potential of the makran
815   subduction zone. Geophysical Research Letters 40, 1528–1533. doi:10.1002/grl.50374.

816   Straume, E.O., et al., 2019. Globsed: Updated total sediment thickness in the world's oceans. Geochemistry, Geophysics, Geosystems 20, 1756–
817   1772. doi:10.1029/2018GC008115.

818   Ulrich, T., Vater, S. Madden, E.H., Behrens, J., van Dinther, Y., van Zelst, I., Fielding, E.J., Liang, C., Gabriel, A.A., 2019. Coupled, physics-based
819   modeling reveals earthquake displacements are critical to the 2018 Palu, Sulawesi Tsunami. Pure and Applied Geophysics 176, 4069–4109.
820   doi:10.1007/s00024-019-02290-5.